Master Thesis:
Fast Response of the Meridional Overturning Circulation to Agulhas Leakage Perturbations

Erik van Sebille

Supervised by Peter Jan van Leeuwen

Institute for Marine and Atmospheric research Utrecht
Utrecht University

September 1, 2005

Abstract

In this thesis, the adiabatic response time of the Meridional Overturning Circulation to the introduction of an Agulhas Ring in the South Atlantic Ocean and the influence of the Mid-Atlantic Ridge on this response is investigated. To this end, a two-layer Primitive Equation model on a sphere was constructed. The ring is a circle-symmetric Gaussian mass of excess water, in cyclogeostrophic balance. To gain some insight in the strength of the response, the Meridional Overturning Circulation is modelled as two regions, one in the northernmost and one in the southernmost part of the basin, where water is exchanged between the layers. The magnitude of the exchange is governed by two different parameterizations. In the first it is related to the difference in zonally averaged pressure difference at the sea surface, between two predestined regions. In the second it is related to the difference between the meridional mass flux in the upper and the lower layer over 40°N.

The Agulhas rings are simulated realistically. The ring signal travels the ocean via consecutively long Rossby waves and western coastal Kelvin waves on the southern hemisphere, equatorial Kelvin waves and eastern coastal Kelvin waves to finally radiate long Rossby basin modes in the northern hemisphere. The modelling of the overturning circulation has been less successful. Although parameter tuning gives consistent results, the model contains some unwanted features that are discussed in detail.

The impact of one Agulhas ring on the Meridional Overturning Circulation is consistent in the two parameterizations. In the first 3 years, the overturning slows down to accelerate beyond the unperturbed situation after that. The introduction of the Mid-Atlantic Ridge in an attempt to short-cut the wave propagation had little influence on the response time. The magnitude of the response is different for the two parameterizations. The pressure gradient driven parameterization yields a 0.05 Sv response, which is independent of the presence or absence of a Mid-Atlantic Ridge. The flux-driven one gives a 0.4 Sv response in a configuration with a ridge, and a 0.15 Sv response when no ridge is present.

Contents

Chapter 1

Introduction

1.1 Problem formulation

The spatial and temporal distribution of temperature and salt over the Atlantic Ocean is determined by many processes. Some of the most important of these are the in and out fluxes of water through the narrow Drake passage and Denmark strait, the interaction with the atmosphere which is related to both cooling and evaporation and tidal mixing on topography and in small eddies which rearranges the distribution of heat and salt.

In this thesis, however, the focus is on two other processes. One is the North Atlantic Deep Water (NADW) formation near Greenland and the associated concept of the Meridional Overturning Circulation (MOC). The other is the mixing of warm and salt Indian Ocean water into the Atlantic near South Africa in the form of Agulhas Leakage.

Both processes are still being investigated and are far from completely understood. One could therefor argue the need to focus on responses between these two mechanisms as opposed to first fully gasping the separate concepts. However, due to the coexistence in the same oceanic basin, the manifestations of both mechanisms will mutually influence each other. It is therefor worthwhile to give attention to the way these two processes interact. This is further enhanced by the large impact which the Meridional Overturning Circulation has on the European climate, as was noticed by e.g. Clark et al. (2002).

The idea of this thesis is to formulate a numerical model, as simple as possible, that can accommodate for both Agulhas Leakage and the Meridional Overturning Circulation. The model can then be integrated on a computer, to yield a dynamic representation of the problem at hand. The focus and interest lies mainly in the significant responses with shortest timescales.

For the MOC to respond it requires some form of baroclinic energy, whereas the energy that is fastest transmitted from an Agulhas ring is barotropic. The model must therefor be able to accommodate for the transformation from barotropic to baroclinic energy. In the real ocean, this is accomplished by both the to-

pography (Munk and Wunch, 1998) and instabilities in the flow. The first of these will be implemented in the model, and this is done in the form of a Mid-Atlantic-Ridge (MAR). This meridional ridge is in the northern hemisphere able to facilitate the transformation of barotropic into baroclinic energy. This can significantly reduce the time required for an Agulhas Leakage perturbation signal to travel the Atlantic Ocean as it can travel as fast barotropic waves until the very end of the journey.

These consideration lead to the following research questions, which will be the main guidance for this thesis:

Research Questions
(1) What is the adiabatic response time of the Meridional Overturning Circulation on the introduction of an Agulhas ring? **(2) What are the dynamical properties of this response?** **(3) How is the magnitude and temporal scale of this response affected by the presence of a meridional topographic ridge on the ocean floor?**

The processes will be highly idealized and parameterized in order to facilitate them in the model. This parameterization and idealization will imply a reduction in the physics. It will therefor be necessary to make a distinction between physical processes that must be captured by the model, and processes that can be omitted since they are of secondary importance. The distinction has to be made without any *a priory* knowledge of the exact responses. It therefor requires a good physical insight into the problem at hand.

1.2 Historical background

In the last few decades, much research has been concentrated on both the Meridional Overturning Circulation and the Agulhas Leakage. The current achievements in these separate fields will be discussed in sections 2.7 and 2.8 respectively. Next to this topical research, there have also been a number of articles in which the relation between the MOC and Agulhas rings is studied. These articles can be considered the starting point of this thesis, and will therefor shortly be discussed here.

In Weijer et al. (1999) and more specifically the follow-up article Weijer et al. (2002) studies of the long timescale relations between South Atlantic sources of buoyancy and the MOC are described. The authors use the Hamburg Large Scale Geostrophic global ocean model to perform calculations on how the overturning strength is affected by changes in the influx of heat and salt

in the Atlantic Ocean. Although the influx is designed to mimic the changing influx through Agulhas Leakage, the model does not, due to the grid size of $3.5 \times 3.5°$, incorporate a dynamic structure that can be related to an Agulhas ring. The time-step of the model is 30 days and this is too large for a ring, which decays in the order of a year (Van Aken et al., 2003). Therefor, the influx is modelled by prescribing a large region in the thermocline of their model, in which the heat and salt, and thereby the density, can be varied. The influx region is compensated by a outflow region of similar shape in the Indian Ocean. The model is forced with mixed boundary conditions at the sea surface and a prescribed wind-profile.

Since the authors use a global model, they can focus on two quantities that are related to the MOC. The first one is the North Atlantic Deepwater Formation, which takes place near Greenland and is in the order of 20 Sv (1 Sv = 10^6 m^3/s). The other quantity is the North Atlantic Deepwater Outflow, the southward flow of water in the lower layers at 30°S, which is in the order of 15 Sv.

The authors slowly (order 500 years) vary the amount of heat and salt in the input region. They find that both the NADW formation and outflow vary accordingly. However, there are two instances at which a non-linear response takes place. The authors can relate this response, which also exhibits hysteresis, to a change in the convective activity of the Atlantic Ocean.

Concerning the dynamical processes that govern the adjustment of the MOC, the authors show that the changing overturning circulation manifests itself almost entirely in the western (viscous) boundary layer of the Atlantic Ocean, yielding a northward flow at a depth of 150 m and a southward flow at 3000 m. The authors claim that the results from this experiment give enough evidence to conclude that "the reopening of the Agulhas gap at the end of the last ice-age may have played a role in the restart of the Atlantic overturning circulation."

The most important result for our research, however, is the linear relation found between the zonally averaged meridional pressure gradient and the NADW production. This result provides a physically motivated implementation of an overturning circulation, which will be used in our model. This is further discussed in section 3.6.1.

Next to the long time-scale experiment, the authors have also conducted an experiment in which they suddenly apply a salt and heat input near the Cape of Good Hope. In order not to destabilize the stratification, the authors make sure that the input is positively or neutrally buoyant. The sudden influx must mimic a fast change in the Agulhas Leakage. Unfortunately, the size of the source modification is too large in order to represent an Agulhas ring. Quantitatively, therefor, the research of Weijer et al. (2002) can not be compared to our research project. Qualitatively, however, it is more useful.

In their diffusivity-driven model, the authors find a distinction in the timescale of the response between an anomaly in the salt and heat flux. There is a lag of 30 years in the response of the overturning strength on an input of salt. This is in good agreement with the advective timescale, in which it takes 30 years to travel 10^7 m with 10^{-2} m/s. The heat anomaly has a much shorter lag on the overturning strength, approximately 2 years according to the model results.

This timescale can only be explained using barotropic waves, since baroclinic waves take at least 6 years to cross the Atlantic Ocean. Since the model is very coarse, this result requires some extra investigation. Although the authors hint at some of the dynamical properties of the response, they can not draw any conclusions due to the large grid spacing and time step. Moreover, since their model has no topography, the possible influence of a Mid-Atlantic Ridge on the response can not be captured in their study.

It must be noted that since the authors use a source region spanning almost the entire width of the Atlantic Ocean, they have a large head-start in the transportation of the density anomaly. Compared to the release of an Agulhas ring near the Cape of Good hope, the long journey of crossing the South Atlantic Ocean is omitted. We shall show that this part of the journey takes 3 years and plays a key role in the overturning response.

Another paper which is relevant for this research is that of Johnson and Marshall (2002b). The authors do not study the response of the MOC to Agulhas rings, but the dynamic response of the ocean to MOC perturbations. Although this might seem far off from the research question, the way in which the authors implement the MOC perturbations provides the model with much relevance. The model has a high resolution, but is implemented as a reduced gravity model, yielding the computation of only one layer (see section 2.1). The perturbation is a localized density anomaly, released at 60°N near the western coast of the Atlantic Ocean. The dynamical properties of the perturbation, with a mix of Kelvin and Rossby waves, might be very alike the dynamical properties of the Agulhas ring. It their model, a consecutive succession of these waves can transmit a signal throughout the basin, and can even pass the equator, thereby connecting the different hemispheres. The authors find a response on the unperturbed hemisphere (here the southern, in our experiments the northern) within 2 years. However, placing the anomaly at the western border gives the same 3 year head-start as in the research by Weijer et al. (2002).

In their article, and in the follow-up (Johnson and Marshall, 2002a), the authors also comment on what they call the *equatorial buffer*. This is a phenomenon that occurs when a perturbation is be transported as an Kelvin wave along the western coast. As the signal moves equator-ward, geostrophy requires a smaller pressure gradient to support the same transport. Therefore, the pressure anomaly (wave) will reduce as it travels towards the equator. This shallower wave will cross the basin as an equatorial Kelvin wave, and will travel along the eastern coast with an amplitude much smaller than it initially had on the western coast. Therefor, the energy that is transported by this Kelvin wave mechanism from the perturbed to the unperturbed hemisphere is only a fraction of that which remains in the perturbed hemisphere. This might be a phenomenon that can affect our experiments, but as long as a significant portion of the (damped) signal is still able to cross the equator, this does not have to frustrate the research.

1.3 Overview of this thesis

The main purpose of this report is to give a survey of the research, through numerical modelling, that was done to investigate the response of the MOC on Agulhas leakage. This investigation was performed with a high resolution two layer model which can facilitate a Mid-Atlantic Ridge. This is in contrast to previous research, in which the response was addressed with a low-resolution flat-bottom model (Weijer et al., 2002) or with a high-resolution reduced gravity model (Johnson and Marshall, 2002b).

Since this report is a master thesis, it will commence in the second chapter with a rather thorough description of the theory needed to understand all the phenomena and results discussed later. The concepts and their theory are described in an independent way, as to facilitate the reader to read through less familiar concepts and to skip the acquainted ones. They include a short introduction to Reduced Gravity and Two-Layer models, Kelvin waves, (topographic) Rossby waves and the kinetic energy of barotropic and baroclinic modes, as well as some basic background knowledge of the MOC and Agulhas Leakage and rings.

The third chapter of this thesis is dedicated to a description of the model. Since the results discussed later come from different modifications of the basic model, this chapter will give a broad idea of all the possibilities entrained in the model. It will also discuss the two different ways in which the actual overturning circulation has been incorporated in the Two-Layer model, something that we do not know any precedent of.

The fourth chapter, then, presents the results as they are obtained from model output. The chapter holds a number of different experiments, which shall be explained, interpreted and discussed in separate sections. A lot of time has been invested in determining the trustworthiness of the model, by some simple experiments. Although they are not very relevant for an answer to the research question, they shall be discussed to place the model in some perspective. After that, the results of the response-experiments shall be presented.

The fifth chapter gives a general discussion on the experiments and the reliability of the results, after which the report ends with a chapter on the conclusions which can be drawn.

Chapter 2

Theory and Concepts

This chapter deals with some of the theory and concepts that are needed to fully appreciate the results of the experiments. The very basics of geophysical fluid dynamics is prerequisited, the rest will briefly be discussed here. Since two different models will be used, the Reduced Gravity (RG) and the Two Layer (TL) model, the theory will be presented in order to describe the dynamics that govern these two models. Most of the derivations are adapted from Gill (1982) and Pedlosky (1987) and will be given without further reference. The two models will first very shortly be discussed, after which Kelvin waves, Rossby waves, Topographic Rossby waves, the Meridional Overturning Circulation and Agulhas Rings will consecutively be treated. The actual implementation and a more extensive discussion is given in section 3.4.

2.1 Reduced Gravity models

The RG-model is a one-and-a-half layer model. An active layer is placed above a passive layer of infinite thickness. The two layers differ in their respective densities. In the configuration of this model, the relative density difference is multiplied by the gravitational acceleration g to yield the reduced gravity

$$g' = g\frac{\rho_2 - \rho_1}{\rho_2} \tag{2.1}$$

where ρ_1 and ρ_2 are the densities in the active and passive layer respectively. The density factor is in our model $\rho' = \frac{\rho_2 - \rho_1}{\rho_2} = 0.002$.

Through isostasy, fluctuation of the sea surface height (SSH) are cancelled in the height of the interface. The pressure anomaly of a positive (negative) SSH-anomaly η_1 is translated in a depression (rise) of the interface η_2, such that

$$\eta_1 + \rho'\eta_2 \equiv 0 \tag{2.2}$$

Note that in this formulation both the positive η_1 and η_2 are directed upward.

Equation (2.2) relates the interface height directly to the SSH. This implies that only one of the two has to be calculated, halving the computational burden. The drawback is that only slow waves, the baroclinic mode, can be represented and integrated. Fast responses can therefor not be expected in this model.

2.2 Two Layer models

A TL-model can carry fast waves. Compared to the RG-model, the lower layer has been turned active. This is done by reducing the depth of that layer from infinity to a finite depth. Isostasy, equation (2.2), is no longer fulfilled. The two layers have to be calculated separately, increasing the computational effort.

The great advantage of this model is that both the barotropic and the first baroclinic mode can be identified from the calculated fields. The barotropic mode is the depth-independent component of a field, while the baroclinic mode depends on depth. For example, the zonal and meridional barotropic equivalent velocities in a two layer model are defined as

$$u_{BT} = \frac{u_1 h_1 + u_2 h_2}{H} \qquad v_{BT} = \frac{v_1 h_1 + v_2 h_2}{H} \tag{2.3}$$

whereas the baroclinic equivalent velocities are defined as

$$u_{BC} = u_1 - u_2 \qquad v_{BC} = v_1 - v_2 \tag{2.4}$$

in which the subscripts 1 and 2 denote the upper and lower layer respectively. The layer depths are denoted by h_i, and the total depth $H = h_1 + h_2$. From the second equation, it follows that if the velocity fields in the two layers are identical, the baroclinic velocity is zero. This represents the depth-dependent character of the baroclinic mode.

The implications of this model, and the previous one, will further be discussed where appropriate throughout the rest of the thesis.

2.3 Kelvin waves

In the presence of some solid ridge (a coast or boundary), a pressure gradient can be sustained perpendicular on that ridge. As water level rises (drops) at the ridge, the pressure gradient is directed away from (toward) the ridge. At the coast, this pressure gradient is balanced by the normal force on the solid earth. Away from the coast, this pressure gradient is balanced by a Coriolis force. This yields a velocity component parallel to the ridge. In very short, this is the principle of a Kelvin wave: the balance between a sustained pressure gradient force and a Coriolis force.

The concept of a Kelvin wave can be quantized by using the linearized shallow-water equations for a flat bottom. At $x = 0$ a meridional ridge acts as the western boundary of the domain. This implies that $u(0) = 0$, and we can

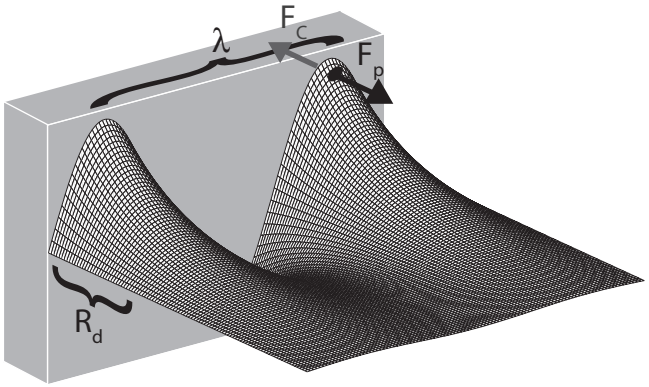

Figure 2.1: The balance behind a Kelvin wave. A pressure gradient force F_p sustained by a coast is balanced by the normal force of the solid earth. Away from the coast, F_p is balanced by a Coriolis force F_C. The length scales are R_d in the zonal and $\lambda = \frac{2\pi}{m}$ in the meridional direction.

look for solutions with a zero zonal velocity $u \equiv 0$ everywhere. This configuration can be represented by the set of equations

$$\begin{aligned} -fv &= -g\frac{\partial \eta}{\partial x} \\ \frac{\partial v}{\partial t} &= -g\frac{\partial \eta}{\partial y} \\ \frac{\partial \eta}{\partial t} + H\frac{\partial v}{\partial y} &= 0 \end{aligned} \tag{2.5}$$

where H is the undisturbed ocean depth, g the gravitational acceleration, f the Coriolis parameter, v the meridional velocity and η the sea surface height.

Solving the coupled set (2.5) for the wave functions $v = v_0(x)e^{i(my-\omega t)}$ and $\eta = \eta_0(x)e^{i(my-\omega t)}$ gives the dispersion relation

$$\omega = \pm\sqrt{gH}m \tag{2.6}$$

and the amplitude of the sea surface height

$$\eta_0 = Ae^{\pm\frac{f}{\sqrt{gH}}x} \tag{2.7}$$

The phase and group velocities can be deducted from equation (2.6)

$$c = \frac{\omega}{m} = \pm\sqrt{gH} \tag{2.8}$$

$$c_g = \frac{\partial \omega}{\partial m} = \pm\sqrt{gH} \tag{2.9}$$

These last three equations reveal all properties of the Kelvin wave that are required for this research. Equation (2.7) shows that although the sea surface

elevation in the meridional direction is wavelike, in the zonal direction it falls off with

$$R_d = \frac{\sqrt{gH}}{|f|} \tag{2.10}$$

the *Rossby deformation radius*. The sign in equations (2.7), (2.8) and (2.9) is determined by the sign of f. The exponent in equation (2.7) must be negative for the solution to stay bounded as $|x| \to \infty$. The force balance is depicted in figure 2.1.

Equation (2.6) shows that the waves are nondispersive, their phase velocity is equal to their group velocity. Again, the sign in equation (2.6) depends on the sign of f, in the same way that the sign of equation (2.7) depends on f. This sign makes that a Kelvin wave always travels in a cyclonic direction.

The entire exercise described above can also be performed for a zonal ridge. This yields the same results, except for the x in equation (2.7) which in the zonal ridge configuration has to be replaced by a y.

A final notion for Kelvin waves is the *equatorial* Kelvin wave. Physically, this is a pair of Kelvin waves on opposite sides of the equator that can maintain a meridional pressure gradient by 'leaning' on each other. As f changes sign at the equator, so does $\frac{\partial \eta}{\partial y}$. This results in a Kelvin wave with equal phase speed and symmetric $\eta(y)$ travelling in an eastward direction.

Concerning the different models, the theory is with minor alterations applicable. In the Reduced Gravity model, the gravitational constant g has to be replaced with the reduced gravity g' as defined in equation (2.1) and η is the deviation of the interface. As the density factor is typically 0.002, this implies a decrease in phase and group velocity to only 4.5% of the shallow water phase velocity.

In the TL-model, both interfaces can carry a wave. The dynamics in the upper one is governed by the original value for g and in the lower one it is governed by g'. The waves on the surface therefor travel much faster than those on the interface between the layers.

2.4 Rossby waves

Just as the Kelvin wave requires a solid ridge, the Rossby wave can not be a solution of the quasi-geostrophic dynamics without the assumption that the Coriolis parameter f varies with latitude. In the primitive equations model the potential vorticity is conserved. This can be written as

$$\frac{d}{dt}\left(\frac{\zeta + f}{h}\right) = 0 \tag{2.11}$$

From this conservation law, the propagation mechanism for short Rossby waves ($L^2 \ll R_d^2$) can be deducted. In this case, equation (2.11) reduces to

$$\frac{1}{h}\frac{d}{dt}\left(\zeta + f\right) = 0 \tag{2.12}$$

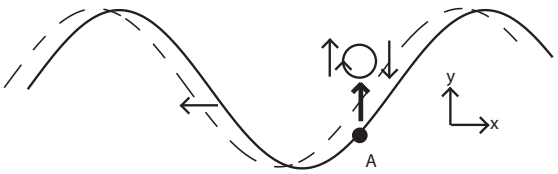

Figure 2.2: The processes behind a Rossby wave. As a point A moves northward, the Coriolis force will change, resulting in a clockwise motion. Particles on the left will be accelerated northward, while those on the east are moved southward. In this way, the wave moves eastward.

As f changes, and the layer thickness h stays constant, the relative vorticity $\zeta = \frac{\partial v}{\partial x} - \frac{\partial u}{\partial y}$ also has to change. Therefor, water particles moving to a region of higher Coriolis-parameter (i.e. northward) must compensate in their relative vorticity. This results in an anticyclonic motion, and it is this motion that will cause a wavelike behavior. As a particle moves anticyclonic, some neighboring particles will be transported northward and some will be transported southward. But as the northward moving particles move into a region of higher f, they will also rotate anticyclonic. The original particle will now be moved back south, and what was originally the wave crest has moved one particle westward. The entire process is captured in figure 2.2.

For long Rossby waves ($L^2 \gg R_d^2$), the potential vorticity reduces to

$$\frac{d}{dt}\left(\frac{f}{h}\right) = 0 \tag{2.13}$$

The propagation mechanism is quite different now. A change in f has to be balanced by a stretching (change in h) of the water column. As a water column moves northward, its surface height will be greater than that of the surrounding water columns. This is accompanied by a geostrophic velocity field along the height contours, resulting in a pole-ward flow west of the water column and an equator-ward flow east of it. The water columns west will have to stretch in order to compensate for the increased planetary vorticity and the water columns east will have to shrink. In this way the wave propagates westward.

The derivation of the phase and group velocity of plane Rossby waves will not be presented here. For instance Pedlosky (1987) gives a good step-by-step derivation. In this section only the results will be given. The zonal and meridional component of the phase speed of plane Rossby waves are respectively

$$\begin{aligned} c^x &= -\frac{\beta}{l^2 + m^2 + 1/R_d^2} \\ c^y &= -\frac{\beta l/m}{l^2 + m^2 + 1/R_d^2} \end{aligned} \tag{2.14}$$

with $\beta = \frac{\partial f}{\partial y}$ the meridional gradient in the Coriolis force and m and l the zonal

and meridional wave-numbers respectively. R_d is the same Rossby deformation radius as in equation (2.10).

The first of equations (2.14) is the most intriguing. As the denominator must be positive, and $\beta > 0$, the zonal phase speed is always westward. Note that this is consistent with the result from the discussion of the propagation mechanism given before. Moreover, for long waves ($|l|, |m| \ll 1/R_d^2$), the phase speed becomes

$$c^x = -\beta R_d^2 \tag{2.15}$$

This is also the maximum phase speed. All others are smaller, illustrating the dispersive nature of Rossby waves.

The zonal *group* velocity, however, does not have to be negative. For zonally short waves, the group velocity can be eastward. To be precise, the group velocity is eastward when $l^2 > m^2 + 1/R_d^2$. As it is the group velocity by which energy is transported, this is an important result for the experiments that will be performed.

Similar to the situation described in the previous section, the only alteration to this theory in order to be applicable to the RG-model which has to be made is a transformation of gravity parameter $g \to g'$ and a reinterpretation of η which is now the interface deviation. This reduces the Rossby deformation radius and through that the dispersion relation. Since R_d is altered, the division-line between long and short Rossby waves also changes. What was first a short (eastward propagating) Rossby wave can become a long (westward propagating) wave in the reduced gravity setting.

The situation in the TL-model is more interesting. Since the two layers are linked via the pressure force, a stretching of one of the layers will alter the thickness of the other. It is therefor possible to couple the two layers into one system. Pedlosky (1987) shows that the baroclinic dispersion relation of a two layer system is

$$\omega = \frac{-\beta l}{l^2 + m^2 + \frac{f^2}{g' h_1} + \frac{f^2}{g' h_2}} \tag{2.16}$$

whereas the barotropic dispersion relation reads

$$\omega = \frac{-\beta l}{l^2 + m^2} \tag{2.17}$$

It can be shown that in a Two Layer system, the volume transport for a baroclinic wave in the upper layer is equal to that in the lower layer, but with a phase shift of 180°. The velocities are always in opposite directions, and this helps to understand the way in which the baroclinic waves move. For short waves, the mechanism is equal to that of the one-layer system, figure 2.2. For long waves, the fact that the water moves in opposite direction is crucial. If water in the upper layer flows northward, the layer will stretch. Since the water in the lower layer will then flow southward, that layer will shrink. The interface

will therefor move down and the neighboring water columns will stretch (west side) and shrink (east side) moving the Rossby wave on the interface westward. The same holds for the surface.

2.5 Topographic Rossby waves

From the conservation of vorticity, equation (2.11), it follows that not only a change in f can account for a change in the relative vorticity. A change in the layer thickness h can also account for the relative-vorticity induced wavelike motion that was described in the previous section. If the layer thickness varies in the meridional direction (a zonal ridge), the problem has been well-studied. The concepts of Coriolis parameter variation and the layer thickness gradient are then interchangeable. They will both result in Rossby wave propagating through the (anti)cyclonic movement of water columns. The direction depends on the sign of the slope. β In equation (2.14) can then be replaced by the slope parameter $\frac{f}{H}h_y$ where H is the undisturbed ocean depth and h_y is the meridional gradient in the ridge height.

In this section, we will concentrate on layer thickness variations in the zonal direction, since that is what is required for the interpretation of the results (waves on the Mid-Atlantic Ridge), later on in this thesis. Using the quasi-geostrophic (QG) theory, we can rewrite the conservation of potential energy, equation (2.11). In this theory, the velocity fields are divergence-free and a streamfunction ψ can be used in the usual way ($u = -\psi_y, \quad v = \psi_x$). Moreover, the layer thickness h can be rewritten as

$$h = H + h_x x \tag{2.18}$$

where $h_x x \ll H$, the depth deviations by the (linear) topographic ridge. Implementing those alterations in the QG-model yields the equation

$$\frac{d}{dt}\left(\Delta_0\psi + f_0 + \beta y - \frac{1}{R_d^2}\psi - \frac{f_0}{H}h_x x\right) = 0 \tag{2.19}$$

where Δ_0 denotes the horizontal Laplacian. This leads to the dispersion relation

$$\omega = -\frac{\frac{f}{H}h_x m + \beta l}{m^2 + l^2 + 1/R_d^2} \tag{2.20}$$

It is possible to derive a similar result for a two layer model. However, since only the lower layer is affected by the ridge, the topographic gradient term only shows in one of the two coupled potential vorticity equations. This yields a very elaborate and unmanageable dispersion relation that does not give any fast physical insight at all. The problem is that a simple decoupling into barotropic and baroclinic modes is not possible due to the bottom topography term. Although the two-layer description is strictly better, we will therefor only focus on the one-layer topographic Rossby waves.

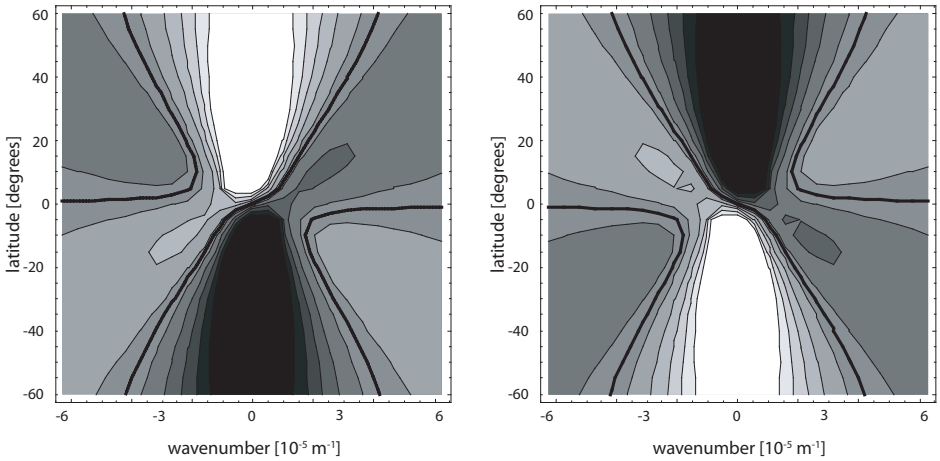

Figure 2.3: The meridional group velocity c_g^y as a function of latitude and meridional wavenumber, for the western side of a mountain ridge, where $h_x < 0$ (left) and the eastern side of a mountain ridge $h_x > 0$ (right). The meridional wavenumber m range is such, that the shortest waves have a wavelength of $\lambda = 100$ km. The zonal wavenumber l is set to $2\pi/(500\text{ km})$, the width of the mountain range as used in the experiments. In the color scale, black is negative (southward) and white positive (northward). The thick black line is the $c_g^y = 0$ isopleth.

We are interested in the way energy is transported along the ridge, and therefor we need an expression for the meridional group velocity:

$$c_g^y = \frac{\partial w}{\partial m} = \frac{\frac{f}{H} h_x (m^2 - l^2 - 1/R_d^2) + 2lm\beta}{(m^2 + l^2 + 1/R_d^2)^2} \tag{2.21}$$

Figure 2.3 plots the meridional group velocity c_g^y as a function of latitude and meridional wavenumber m. The zonal wavelength is taken to be $\lambda = 2\pi/l = 500$ km, the width of the ridge that will be used in the experiments. Although the quantitative usefulness of the figure is limited, the qualitative insight it gives is very useful. For long waves, the group velocity is pole-ward on the western and equator-ward on the eastern slope of a ridge. Beyond some wavelength, this direction flips and short waves travel equator-ward on the western and pole-ward on the eastern slope. Apparently there is a separation in the properties of long and short waves that is dependent of latitude but is in the order of $\lambda = \mathcal{O}(200\text{ km})$.

Another remark can be made on the role of the equator. Both long ($m < 1 \cdot 10^{-5}$ m^{-1}) and short ($m > 2 \cdot 10^{-5}$ m^{-1}) waves experience a change in the sign of c_g^m as they pass the equator. There is however a subset of wavenumbers for which the zero-group velocity isoline has an offset from the equator. There are therefor topographic baroclinic Rossby waves that can pass the equator, if their wavenumber is just such that they fall in the gaps of the zero-isopleth at

$\theta = 0°$. These waves can transmit energy as far as 20° beyond the equator, effectively coupling the hemispheres.

2.6 Energetics of barotropic and baroclinic modes

For further reference, the expressions for the barotropic and baroclinic kinetic energy will be given here. As the experiments will use Two-Layer models, there will be one barotropic and one baroclinic mode. It is important to distinguish between those two, as only the baroclinic mode is thought to be capable of influencing the overturning circulation by the antiphase coupling between the upper and lower velocity field.

In the expressions, we shall use that H_1 and H_2 are the undisturbed layer depths of the upper and lower layer respectively. Moreover, η_1 and η_2 are the interface elevations of the upper and lower layer, both negative towards the ocean bottom. Then $H = H_1 + H_2 + \eta_1$ is the total ocean depth and $h_1 = H_1 + \eta_1 - \eta_2$ and $h_2 = H_2 + \eta_2$ are the layer thicknesses.

To determine the kinetic energy, it is assumed that $\rho_1 = \rho_2 = \rho$, the densities in the layers do in first order not differ (the boussinesq approximation). With this notation, we can write for the total kinetic energy of the system per unit surface area

$$E^{kin} = \frac{1}{2}\rho h_1 \left(u_1^2 + v_1^2\right) + \frac{1}{2}\rho h_2 \left(u_2^2 + v_2^2\right) \tag{2.22}$$

where (u_1, v_1) are the velocities in the upper and (u_2, v_2) are the velocities in the lower layer. For the barotropic kinetic energy we can write

$$E_{BT}^{kin} = \frac{1}{2}\rho H \left(u_{BT}^2 + v_{BT}^2\right) \tag{2.23}$$

in which u_{BT} and v_{BT} are given by equation (2.3). Combing these two equations yields an expression for the baroclinic kinetic energy

$$E_{BC}^{kin} = E^{kin} - E_{BT}^{kin} = \frac{1}{2}\rho \left[\frac{h_1 h_2}{H}\left(u_{BC}^2 + v_{BC}^2\right)\right] \tag{2.24}$$

with the baroclinic velocities, u_{BC} and v_{BC} as given in equation (2.4).

2.7 The Meridional Overturning Circulation

The Meridional Overturning Circulation, of which the North Atlantic Deep Water Formation is a component, is the zonally averaged oceanic circulation with enhanced downwelling in the northern Atlantic Ocean. Although the exact mechanism behind the Meridional Overturning Circulation (MOC) is still disputed (see e.g. Rahmstorf (1996)), the forcing is thought to be the meridional density difference in the Northern Atlantic. As the surface water flows northward, it is cooled and its salinity is increased by the excess evaporation under

the warm atmosphere. This causes surface waters with densities among the highest in the world (Levitus, 1982). As the surface waters reach the northernmost Atlantic, they sink to form the North Atlantic Deep Water. The heavy water flows back southward and leaves the Atlantic basin near South-Africa. The deep water then flows to the Indian and Pacific Ocean. During its journey, the deep water slowly mixes with the surface waters. Together with upwelling in the Antarctic Circumpolar Current, this re-entraines the deep water back into the surface waters. As this happens, the surface waters flow back to the northern Atlantic Ocean and the overturning circulation is complete (see e.g. IPCC (2001)).

The circulation strength is estimated to be 15±2 Sv, where 1 Sv = 10^6 m^3s^{-1} (Ganachaud and Wunch, 2000). The heat flux that this brings about in the northern Atlantic is 1.3 PW (Ganachaud and Wunch, 2000), warming Europe by approximately 10 K (Rahmstorf and Ganopolsky, 1999). Changes in the MOC are therefor thought to have great implications on the (European) climate, and this is one of the reasons that an active field of research has developed (see e.g. Clark et al. (2002)).

2.8 Agulhas Rings

In the surface return flow of the Meridional Overturning Circulation, Agulhas rings are the link between the Indian and the Atlantic ocean (Gordon, 1986). As the warm and saline western intensified Agulhas current flows poleward towards the Cape of Good Hope, it forms a retroflection current near the Cape. In this retroflection, Agulhas rings can be shed as large eddies (De Ruijter et al., 1999). These eddies, which are Indian Ocean water masses in the surrounding Atlantic Ocean, are thought to play a crucial role in the total Meridional Overturning Circulation. In their variability, they form a key link in climate change processes such as (de)glaciations (Knorr and Lohmann, 2003; Peeters et al., 2004).

The number of Agulhas rings that shed every year is approximately six, and each accounts for a volume flux between 0.5 and 1.5 Sv (De Ruijter et al., 1999). The rings vary not only in their size, but also in the location of their origin. The paths they follow through the Atlantic vary as well, but in general rings have been encountered between 20°S and 40°S, with the bulk around 30°S. In general, the rings are move from the cape of Good Hope at 35°S to 30°S along the African coast, after which they move northwestward to the Brazilian coast. Some of the rings can be monitored all the way to the coast of Brazil. However, the large majority of the rings decays much earlier (Schouten et al., 2000).

The rings are encountered as anticyclones, having a positive sea-surface anomaly. Van Aken et al. (2003) thoroughly describe one of the Agulhas rings, named 'Astrid'. The maximum velocity of this ring is 1.0 m/s at the surface, and an anticyclonic velocity can be measured all the way through the ocean interior. This implies that the ring extends toward the ocean floor. The maximum sea surface elevation is 70 cm which makes Astrid, according to the authors, a large ring.

The mechanisms governing Agulhas ring shedding are still very much under the attention of researchers. The topography around the southern tip of Africa (the Agulhas Ridge, see Schouten et al. (2000)) plays a large role in the shedding, as do the Natal-pulses that run along the eastern side of Africa (Van Leeuwen et al., 2000; Schouten et al., 2002). However, this research will focus on the disintegration of Agulhas rings in the Atlantic, instead of the formation. The subtleties of this last process will therefore be put aside.

Finally, it must be noted that an Agulhas ring by itself can also behave like a Rossby wave. As the ring resembles a sea surface anomaly, the water columns are stretched more in the center of the ring, than near the edges. This stretching accounts for a change in layer thickness, the h-term in equation (2.11). The sea surface perturbation will therefor have similar characteristics as a Rossby wave over a zonal ridge, where a change in h causes the relative-vorticity induced motion. The entire ring can therefor be treated as a superposition of Rossby waves with different length. The nonlinearities in this superposition prohibit the ring from quickly disintegrating in different Rossby waves with different (group)velocities. The nonlinearity is therefor essential for the ring to maintain its structure.

Chapter 3

The Model

The model as used in this research is an extension of a Primitive Equations Reduced Gravity model written by P. J. van Leeuwen (personal communication) to study the coupling between wind and oceanic flow. Since nothing has been published yet about this specific model, it has to be extensively commented on. We will deal with both the theoretical principals behind the model, as with the actual implementation.

3.1 Governing equations

The governing equations in this model are the primitive equations for a layer i, written in the vorticity form and with a continuity equation of the mass balance in flux form:

$$\begin{aligned} \frac{\partial u_i}{\partial t} - v_i(\zeta_i + f) + \frac{1}{2}\frac{\partial(u_i^2 + v_i^2)}{\partial x} &= -P(x) + D\left(\frac{\partial^2 u_i}{\partial x^2} + \frac{\partial^2 u_i}{\partial y^2}\right) \\ \frac{\partial v_i}{\partial t} + u_i(\zeta_i + f) + \frac{1}{2}\frac{\partial(u_i^2 + v_i^2)}{\partial y} &= -P(y) + D\left(\frac{\partial^2 v_i}{\partial x^2} + \frac{\partial^2 v_i}{\partial y^2}\right) \\ \frac{\partial h_i}{\partial t} &= \frac{\partial u_i h_i}{\partial x} + \frac{\partial v_i h_i}{\partial y} \end{aligned} \tag{3.1}$$

in which $\zeta_i = \frac{\partial v_i}{\partial x} - \frac{\partial u_i}{\partial y}$ is the relative vorticity and D the viscosity coefficient. The pressure term $P(k)$ is formulated as

$$P(k) = \begin{cases} g\frac{\partial \eta_1}{\partial k} & \text{for layer 1} \\ g\frac{\partial \eta_1}{\partial k} + g'\frac{\partial \eta_2}{\partial k} & \text{for layer 2} \end{cases} \tag{3.2}$$

The interface elevation η_i is related to the layer thickness h_i through

$$h_i = \eta_i - \eta_{i+1} + H_i \tag{3.3}$$

with the condition that if the model contains n layers, then $\eta_{n+1} = 0$. H_i is the undisturbed layer thickness.

The somewhat unorthodox way in which the advection terms are treated in equation (3.1) is done for the purpose of extra stability. Note that (dropping the subscript i)

$$\begin{aligned} -v\zeta + \frac{1}{2}\frac{\partial(u^2+v^2)}{\partial x} &= -v\frac{\partial v}{\partial x} + v\frac{\partial u}{\partial y} + u\frac{\partial u}{\partial x} + v\frac{\partial v}{\partial x} \\ &= u\frac{\partial u}{\partial x} + v\frac{\partial u}{\partial y} \end{aligned} \tag{3.4}$$

The same argument can be used with the second equation. The form of equation (3.1) is therefor fully equivalent to the more orthodox models that deal with advection in the form of the last terms in equation (3.4). It is not uncommon for the advection in multi-layer models to be defined in this way.

3.2 Boundary conditions

3.2.1 Geometry

As for any model, the governing equations can only be solved when appropriate boundary conditions are prescribed. As we attempt to describe processes in the Atlantic Ocean, the obvious choice would be to use the geometry and bathymetry of the actual oceanic basin.

If this were the road to follow, the model would become very complex, not only in its implementation but also in the interpretation of the results. The goal of this research is to comment on a one-to-one relation between Agulhas leakage and the Meridional Overturning Circulation, and relations between those processes can best be studied when as little as possible processes interfere. Off course, this can also mean that potentially important interactions (focussing, resonance) are left out but in view of a simple model and interpretation this is the price that has to be paid. Therefor the goal should be to write down a set of boundary conditions which on the one hand give an appropriate representation of the situation in the Atlantic Ocean, and on the other hand limit the occurrence of processes other than the ones we are interested in through the problem formulation.

The North Atlantic Deepwater Formation occurs in the very northernmost part of the Atlantic, near Greenland. The northern boundary should therefor be situated at these latitudes, $\theta = 60°\text{N}$. The model must on the other hand also facilitate the Agulhas Rings, which typically occur at $\theta = 30°\text{S}$. This would suggest a southern boundary of the model at $\theta = 30°\text{S}$. However, the MOC must also have a region of upwelling for the total mass balance to become zero.

Present day notion locates this region of upwelling in the North Pacific, the Indian Ocean and the Antarctic Circumpolar Current (IPCC, 2001). Including these regions in the model would require a Global Circulation Model, and this would heavily increase the computational effort. A better way to incorporate overturning upwelling is to extend the southern boundary southward of the

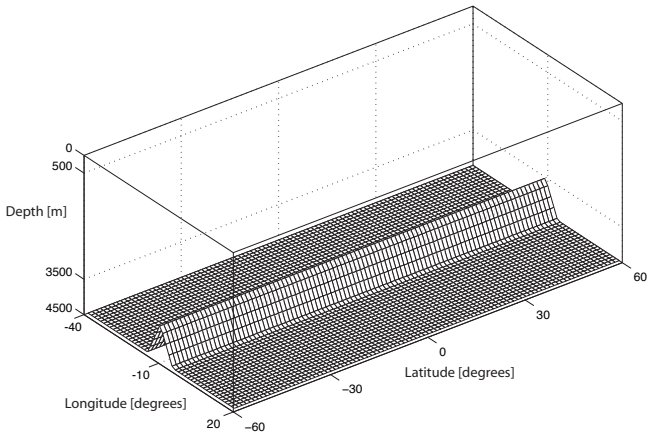

Figure 3.1: The geometry and bathymetry of the model used. The northern and southern boundaries are at $\theta = 60°N$ and $\theta = 60°S$ respectively. The distance between the eastern and western boundary is 60° as they are located at $\phi = 40°W$ and $\phi = 20°E$. The model consists of two layers, one 500 m *thick and one* 4000 m *thick. In the one-layered reduced gravity model, the last layer is set to infinite thickness. The (optional) Mid-Atlantic Ridge is centered between the eastern and western boundary and has a maximum height of* 1000 m*, dropping off linearly to zero over 5°.*

Agulhas ring release region, giving enough room for a return flow in the south. The southern boundary is therefor located at $\theta = 60°$S.

As for the eastern and western border, two straight zonal boundaries were chosen. The distance between those two is 60°, one at $\phi = 40°$W and one at $\phi = 20°$E. The choice of the exact location of these zonal borders obviously does not alter the results of the experiments.

The depth is not constant over the entire basin, but will depend on the experiment at hand. To model the Meridional Overturning Circulation, we need at least two layers, one top layer for the northward transport of the surface water and one lower layer to accommodate the return flow in the abyssal ocean. The upper layer is 500 m thick, and the lower 4000 m.

Some experiments require the presence of a Mid-Atlantic Ridge. This ridge is parameterized by a wedge-shaped obstacle on the ocean floor, uniform in the meridional direction. The maximum height is 1000 m, falling linearly to zero over 500 km. The ridge is located halfway between the eastern and western boundary, its maximum at $\phi = 10°$W.

The entire configuration of the geometry and bathymetry of the basin is depicted in figure 3.1. For convenience, one degree is set equal to 100 km in both meridional and zonal direction, independent of latitude.

3.2.2 Parameters

We expect Rossby waves to play an important role in the energy transfer from the eastern to the western coast of the ocean. To sustain such Rossby waves, a Coriolis parameter that varies with latitude is needed (see also section 2.4). One way to do this is to use a first order approximation to the Coriolis parameter, the β-plane approximation.

In this model, however, we use the full Coriolis parameter $f = 2\Omega \sin(\theta)$ (with Ω the angular speed of the Earth's rotation) instead of the β-plane approximation. The meridional size of the domain is too large for this approximation to be appropriate.

In view of this meridional size, it should be noted that the curvature terms *have* been left out of the primitive equations. It might seem inconsistent to leave out curvature but to include the full Coriolis parameter. However, the model still fulfills the basic conservation laws (mass, momentum and angular momentum). Qualitatively, the model is therefor correct. The quantitative results can be altered by the choice of using the full Coriolis parameter, but we feel that this is of minor importance.

The primitive equations (3.1) are stated in terms of the three fields h, u and v: the layer thickness, the zonal velocity and the meridional velocity. These fields need prescribed values on the geometric boundaries for them to be solved in the total domain.

A distinction between the eastern and western boundary on the one hand and the northern and southern on the other hand has to be made. The eastern and western boundary are closed, representing the American and European/African continents. A logical boundary condition would be the no-slip condition, where all velocities have to be zero at the coasts. At the northern and southern boundary we encounter an open ocean. A natural condition here would be the free-slip condition. The perpendicular component (v) must vanish and there can not be any sheer in the parallel component (u). These two boundary conditions can be formulated as

$$\begin{aligned} u = v = 0 \qquad & \text{for} \quad \theta = \{60^\circ \text{ N}, 60^\circ \text{ S}\} \\ \frac{\partial u}{\partial y} = v = 0 \qquad & \text{for} \quad \phi = \{40^\circ \text{ W}, 20^\circ \text{ E}\} \end{aligned} \tag{3.5}$$

3.2.3 Damping on the southern boundary

The way in which the northern and southern boundaries are implemented in the model allows for Kelvin waves to be guided along these boundaries. A pressure gradient can build on the boundaries, and through this pressure gradient a geostrophic equilibrium can be maintained, resulting in a Kelvin wave (see section 2.3).

In the Southern Atlantic Ocean, there is no such boundary. The Atlantic connects to the Southern Ocean and there will be no waveguides. Zonal Kelvin waves will therefor never be present in the Southern Atlantic Ocean. Since the

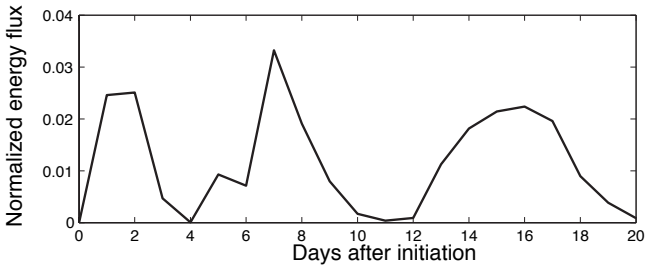

Figure 3.2: The flux of barotropic energy through the southernmost 125 km *of the model at 10° W. The flux is normalized to the total barotropic energy flux over that longitude.*

objective of the experiment is to study the transfer of energy through waves in an idealized Atlantic Ocean, waves that cannot be present in nature should not be represented in the model.

One way to solve the problem of phantom Kelvin waves on the southern border is to implement a Newtonian Filter. This is an extra term in the primitive equations:

$$\begin{aligned}
\frac{\partial u_i}{\partial t} - v_i(\zeta_i + f) + \frac{1}{2}\frac{\partial (u_i^2 + v_i^2)}{\partial x} &= -P(x) + D\left(\frac{\partial^2 u_i}{\partial x^2} + \frac{\partial^2 u_i}{\partial y^2}\right) - \boldsymbol{r u_i} \\
\frac{\partial v_i}{\partial t} + u_i(\zeta_i + f) + \frac{1}{2}\frac{\partial (u_i^2 + v_i^2)}{\partial y} &= -P(y) + D\left(\frac{\partial^2 v_i}{\partial x^2} + \frac{\partial^2 v_i}{\partial y^2}\right) - \boldsymbol{r v_i} \qquad (3.6) \\
\frac{\partial h_i}{\partial t} &= \frac{\partial u_i h_i}{\partial x} + \frac{\partial v_i h_i}{\partial y}
\end{aligned}$$

where only the last term in the first two equations differs from the primitive equations (3.1). The parameter r (units s^{-1}) controls the effectiveness of the damping.

Implementation is done by designating a region of the domain where this damping is applied (Hibiya et al., 1999; Kantha and Clayson, 2000). The parameter r is linearly increased from zero to the typical frequency of the waves to be damped. However, this approach is valid for the different modes (barotropic and baroclinic) and not for the layers. This requires mode-splitting of the velocity fields, after which the separate modes can be damped with their appropriate damping parameter. After severe testing we decided not to implement the mode-splitting

To test the relevance of the Newtonian filter, a calculation is performed. We investigate which part of the total energy transfer is contributed by Kelvin waves on the southern boundary. For the barotropic energy in the domain, the energy flux over 10°W has been computed, for the first 20 days of the model run. This is the time-span when we expect the fast Kelvin waves to be important. It turns out that only 2% to 3% of the total energy flux flows through the southernmost 125 km at any moment (see figure 3.2). The amount of baroclinic energy that

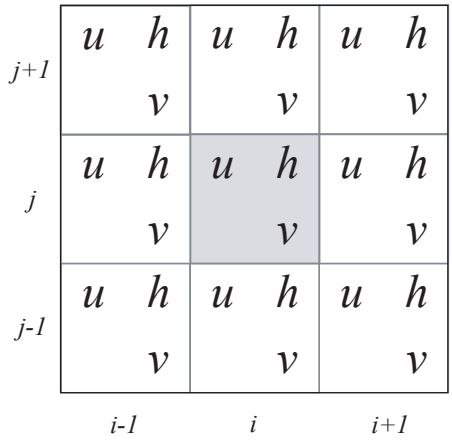

Figure 3.3: The Arakawa C grid as used in the model. At each grid-point (i, j) the height h, the zonal velocity u and the meridional velocity v are calculated. The shaded region resembles one grid-point, with a square size Δ^2

passes through this latitude is even smaller, never exceeding 1% of the total baroclinic flux over 10°W in the first 200 days (not shown). From this, we can conclude that implementing a Newtonian filter on the Southern boundary of the domain is not required. Although it is formally better, there is no evidence that large amounts of energy are transported by Kelvin waves along the Southern boundary.

3.3 Grids and implementation

3.3.1 The Arakawa C-grid

The set of primitive equations (3.1) with the boundary condition equations (3.5) is run on a computer using an Arakawa C grid spacing (Mesinger and Arakawa, 1976; Kowalik and Murty, 1993).

This type of grid is especially useful for geophysical purposes. A C-grid provides every grid point with four cells. Three of these contain the fields that need to be calculated (u, v, h), see also figure 3.3. All cells are identified by a pair (i, j), the grid number in the x-direction and in the y-direction respectively. The distance between grid points is Δ, both in zonal and in meridional direction. The distance between two different fields, for example a h_i and a u_{i+1} is $\frac{1}{2}\Delta$.

The decision to use the C grid spacing has been based on the Rossby deformation radius. As opposed to the other well-known Arakawa grid, the B grid, the C grid performs good when the grid distance Δ is smaller than or of the order of the Rossby deformation radius. The B grid on the other hand, performs better on coarse models ($\Delta \gg R_d^2$), which are often used in long time scale climate models.

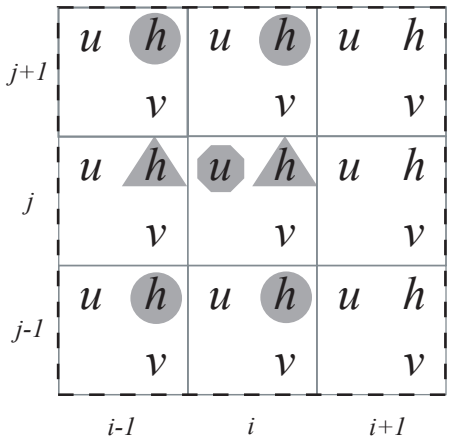

Figure 3.4: The way in which the geostrophic and gravitational balances in the zonal direction are modelled. In order to calculate the geostrophic value for an u-point (octagon), the values of four h-points (circles) are needed. The calculation of the gravitational balance at a u-point requires only the values of two h-points (triangles).

The grid geometry as shown in figure 3.3 reveals why a small grid parameter $d = \Delta/R_d$ performs better on a C grid than on a B grid. On the C grid, the representation of the Coriolis balance $fu = -\frac{\partial h}{\partial y}$ requires information on four layer thickness points, see also figure 3.4. Consequently, the representation of the Coriolis force is not ideal on a C grid. Gravity waves however, can be represented much better. The balance $\frac{\partial u}{\partial t} = -g\frac{\partial h}{\partial x}$ requires the gradient between only two h-points.

If the grid size is smaller than the Rossby deformation radius, the Coriolis force is unimportant on grid level. It will be the gravity waves that play a role on that scale. In this experiment, there are two different deformation radii: the baroclinic and the barotropic deformation radius. The values at mid-hemisphere latitudes (30°S) are respectively

$$R_d^{BC} = \frac{\sqrt{g' H_1}}{|f|} = 43 \text{ km} \tag{3.7}$$

$$R_d^{BT} = \frac{\sqrt{g(H_1 + H_2)}}{|f|} = 2.9 \cdot 10^3 \text{ km} \tag{3.8}$$

which are both greater than the intended grid distance $\Delta = 25$ km. This justifies the use of the Arakawa C grid as the grid for performing the model calculations.

3.3.2 The numerical scheme

The set of primitive equations (3.1) has to be integrated to obtain the dynamical properties of the model. For this purpose, a leap-frog scheme is used. The leap-frog scheme is a computational scheme that requires information about the

state of the model from time $t-1$ when calculating for time $t+1$. Advantage of such a model is that it is more stable compared to an Euler forward scheme (requiring information on time t when calculating for time $t+1$) and that the implementation is relatively easy. Disadvantage is that for the first step $t=1$, the leap-frog scheme can not be used since there is only knowledge on the state of the model on time $t=0$, the initial condition. The first step therefor requires the use of an Euler forward scheme. On the Arakawa C-grid, the first equation from the set of primitive equations (3.1), is implemented as:

$$TotU_{i,j}^{t+1} = \sqrt{(u_{i+1,j}^t)^2 + (u_{i,j}^t)^2 + (v_{i+1,j}^t)^2 + (v_{i,j}^t)^2} \tag{3.9}$$

$$\zeta_{i,j}^{t+1} = \frac{\frac{v_{i,j}^t - v_{i-1,j}^t - u_{i,j}^t + u_{i,j-1}^t}{\Delta} + f_j}{h + 1/4(h_{i,j}^t + h_{i-1,j}^t + h_{i,j-1}^t + h_{i-1,j-1}^t)} \tag{3.10}$$

$$Fv_{i,j}^{t+1} = v_{i,j}^t(h + 1/2(h_{i,j}^t + h_{i,j-1}^t)) \tag{3.11}$$

Resulting in the leap-frog step

$$\begin{aligned} u_{i,j}^t = u_{i,j}^{t-2} - 2\Delta t\Big(g' & \frac{(h_{i,j}^{t-1} - h_{i-1,j}^{t-1}) - \frac{1}{4}(TotU_{i,j}^t - TotU_{i-1,j}^t)}{\Delta} \\ & + \frac{1}{8}(Fv_{i,j}^t + Fv_{i-1,j}^t + Fv_{i,j+1}^t + Fv_{i-1,j+1}^t)(\zeta_{i,j}^t + \zeta_{i,j+1}^t) \\ & + \frac{D}{\Delta^2}(u_{i+1,j}^{t-2} + u_{i-1,j}^{t-2} + u_{i,j+1}^{t-2} + u_{i,j-1}^{t-2} - 4u_{i,j}^{t-2})\Big) \end{aligned} \tag{3.12}$$

The diffusion term is implemented using an Euler forward scheme.

For Δt and Δ, the time step and horizontal grid distance respectively, we need the Courant-Friedrichs-Lewy (CFL) criterium (Mesinger and Arakawa, 1976). This states that for the model to be *stable* it needs to fulfill the inequality

$$\Delta t < \frac{\Delta}{c} \tag{3.13}$$

where c is the phase speed of the fastest waves expected to be encountered.

3.3.3 Boundary conditions

As for the boundary conditions, these can be modelled by applying the equations (3.5). However, due to the spacing of the variables on the C grid, there is no possibility to draw a vertical or horizontal line representing the boundary that encompasses a value for both u and v at the same time. One of the velocity components must therefor be represented by a 'ghost' value. Since interpolation is preferred above extrapolation this requires averaging of two adjacent values for the velocity field.

For the western boundary, one way to do this is to move the boundary one grid point to the right, setting the boundary effectively at $i=2$, as can be seen in figure 3.5. If this is done, and we use that $1/2(v_{1,j} + v_{2,j}) = v_{b,j} = 0$ (where

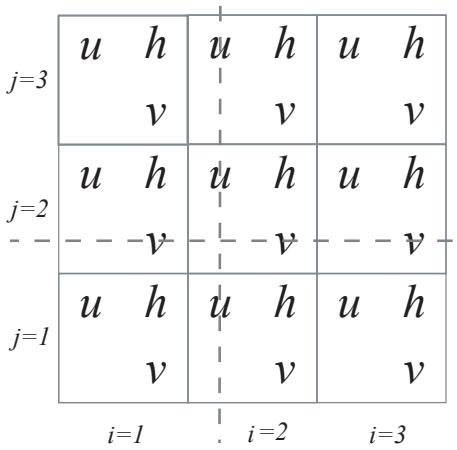

Figure 3.5: The southern and western boundary in the C grid. The actual boundaries are shifted in such a way that all variables can be interpolated to the value on the boundary. The boundaries are represented by the dashed lines.

$v_{b,j}$ is the 'ghost' value on the boundary), the boundary conditions become

$$u_{2,j} = 0 \quad \wedge \quad v_{1,j} = -v_{2,j} \qquad \forall j \tag{3.14}$$

The same arguments apply to the eastern boundary. For an $m \times n$ total grid (m zonal grid points and n in the meridional direction), the boundary condition becomes

$$u_{m-1,j} = 0 \quad \wedge \quad v_{m-1,j} = -v_{m,j} \qquad \forall j \tag{3.15}$$

The no-slip condition at the western and eastern border also sets the total mass flux vh in the meridional direction to zero. The mass flux is calculated at a layer thickness (h) cell, resulting in

$$(vh)_{i,j} = \frac{1}{2}(v_{i,j} + v_{i,j+1})h_{i,j} \tag{3.16}$$

Using the interpolation between the first and second grid point from the boundary and equation (3.14), the boundary condition for the layer thickness at the western and eastern boundary becomes

$$h_{1,j} = h_{2,j} \quad \wedge \quad h_{m-1,j} = h_{m,j} \qquad \forall j \tag{3.17}$$

where the identity for the 'ghost' flux cell $(vh)_{b,j} = 0$ has been used.

The same procedure can be used to obtain constraints for the northern and southern boundaries. At these boundaries, the free slip condition is valid, implying $\frac{\partial u}{\partial y} = 0$. The actual numeric conditions then become (with $\frac{\partial uh}{\partial x} = 0$)

$$u_{i,1} = u_{i,2} \quad \wedge \quad v_{i,2} = 0 \quad \wedge \quad h_{i,1} = h_{i,2} \qquad \forall i \tag{3.18}$$

$$u_{i,n-1} = u_{i,n} \quad \wedge \quad v_{i,n-1} = 0 \quad \wedge \quad h_{i,n-1} = h_{i,n} \qquad \forall i \tag{3.19}$$

The boundary conditions, (3.14), (3.15), (3.17), (3.18) and (3.19) make up the full system of boundary conditions. They are easy to implement and fast to calculate. A drawback is that they decrease the oceanic domain effectively from $m \times n$ to $(m-2) \times (n-2)$. Moreover, the boundary conditions have been derived using a number of interpolations, a method that increases errors while integrating the velocity and layer thickness fields. However the discretisation error due to these interpolations is second order in Δ, just as the errors in the dynamical equations by the use of the Leap-Frog scheme.

3.4 The different models

Up to now the discussion of the model has been generic in the sense that it can be applied to both the Reduced Gravity (RG) and the Two Layer (TL) model. Both models will be used during the experiments, and are therefor shortly discussed.

3.4.1 The Reduced Gravity model

The Reduced Gravity (RG) model has already been treated in section 2.1. The name is derived from the modification of the gravitational constant by a density factor describing the relative difference between the densities of two layers on top of each other. Through the use of isostasy, the velocity and thickness fields in only one of these layers has to be calculated. In this model we use that

$$\rho' = \frac{\rho_2 - \rho_1}{\rho_2} = 0.002 \tag{3.20}$$

The choices to be made concern the horizontal grid size Δ and the corresponding integration time step size Δt. The grid size is a trade-off between accuracy, computational speed and domain size. As argued before, the domain size is chosen to be 120° by 60°. This leaves the grid size and the computational effort open. The grid size has to be small enough to carry the waves we are interested in. As these waves have a wave length $\lambda \sim \mathcal{O}(100 \text{ km})$, a grid size of $\Delta = 25$ km is chosen. For convenience, one degree is approximated to 100 km, implying a total domain of 480×240 grid points.

From the CFL-criterium, equation (3.13), we can now determine the time step to be taken. The fastest waves in the system are the baroclinic Kelvin waves, which have a phase speed of

$$c = \sqrt{g'H} = 3.1 \text{ m/s} \tag{3.21}$$

since the layer depth is 500 m. This yields a time step of $\Delta t = 8.0 \cdot 10^3$ s. The time step that is associated with the diffusion (where $D = 100$ m^2/s is the diffusion parameter)

$$\Delta t \leq \frac{\Delta^2}{2D} \tag{3.22}$$

is even larger at $\Delta t \leq 3.1 \cdot 10^6$ s. However, tests with the model have shown that the model is only stable when the time step is smaller than 900 s. It is unclear why there is such a large difference between the theoretical and experimental maximum time step. It is common practice in oceanographic modelling to decrease the time step a little (typically $\mathcal{O}(90\%)$ of original time step) but the large decrease required in this model is very rare.

3.4.2 The Two-Layer model

Although the RG-model is fast, it is not as accurate as it could be for this research. A better options is to use a multi layered model, the TL-model. This model has been introduced in section 2.2. The lower layer thickness has now been reduced from infinity to 4000 m. The value for ρ' is unchanged, see equation (3.20). As the primitive equations (3.1) have to be solved in both the upper and lower layer, the computational effort will increase. The layers are coupled through the horizontal pressure gradient term and the mass continuity term. The total mass in the layers can however not change, disallowing for transport between the layers.

Gill (1982) shows that in a two layered system both a barotropic and a baroclinic mode can be identified. As opposed to the RG-model, this model does therefor include the fast barotropic waves that are required for the quasi-geostrophic adjustment (see Mesinger and Arakawa (1976)).

In our implementation, the primitive equations are solved one at a time. The velocity fields in the upper layer are calculated first, after which the velocity fields in the lower layer are calculated. The layer thicknesses are calculated last, first for the upper and then for the lower layer. After that, the time increases and the entire calculation scheme is re-applied. To achieve the best possible accuracy, the fluxes in the numerical scheme (equation (3.9)) are recalculated using the latest values of the fields. In that way, the meridional velocity field always addresses the values of the latest zonal velocity field.

Note that the different layers are coupled through the pressure gradient term in the primitive equations. For this, the layer thicknesses have to be rewritten to a sea surface height (upper layer) or interface elevation (lower layer). Both are defined as positive when upward.

The grid distance is equal to that in the reduced gravity model, $\Delta = 25$ km. Since surface gravity waves are now present, equation (3.20) shows that the time step has to be decreased by a factor 22 to 40 s. At this time step size, the model is stable.

Model runs show that in our implementation, mass is always conserved. The deviation in mass is never larger than 1% of the total mass in a layer. This is a results that increases the trust that can be given to the model. Of course, mere mass conservation is not enough to rely on a model, but as the next chapter shows, there is much more evidence to believe in a correct implementation.

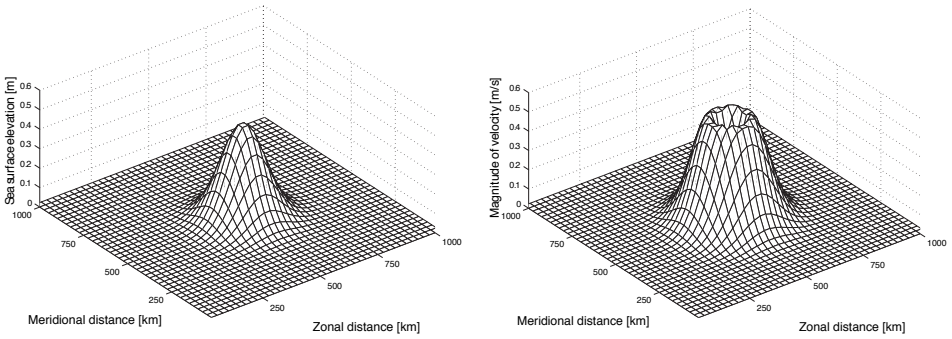

(a) (b)

Figure 3.6: The sea surface elevation of an Agulhas ring (a) and the magnitude of the velocity profile of that same ring in the upper layer (b). The direction of the velocity is such that the ring rotates anti-cyclonic (anticlockwise since the ring is located on the southern hemisphere).

3.5 Implementation of Agulhas rings

In reality Agulhas rings are shed from the Agulhas retroflection area (De Ruijter et al., 1999). This is a very complex process resulting in a large variance in typical sizes and structure of the rings. The structure also varies in both the horizontal and vertical direction. The location at which the rings enter the Atlantic Ocean (are shed from the Agulhas current) is also different for every ring. There is simply no such thing as *the* Agulhas Ring. It is therefor important to parameterize the rings, in such a way that the ring used in the models stands for a wide variety of rings observed in the Atlantic Ocean. It's starting location must also be idealized.

The Agulhas ring in the TL-model is implemented using a Gaussian-shaped mass perturbation, just as was done by Kamenkovitch et al. (1996). The Gaussian has an e-folding scale of 125 km and manifests itself as an anticyclone in both the upper and lower layer. The maximum sea surface elevation is 50 cm. See for the profile figure 3.6(a). Since the relative density difference between the upper layer and lower layer is $\rho' = 0.002$ (see equation (3.20)), a total isostatic balance using equation (2.2) of the maximum sea surface elevation would require a maximum interface depression of 250 m. The maximum depression of the interface is set at merely 200 m. This yields a discrepancy in the isostatic balance, resulting in a total positive pressure force in both the upper and lower layer. Via geostrophy, this results in a anti-cyclonic motion in the ring. All values are taken as they represent a typical Agulhas ring (Van Aken et al., 2003; Drijfhout et al., 2003).

As the ring is Gaussian-shaped, it can be initialized by prescribing both the layer thicknesses and appropriate geostrophic velocity fields. However, this

results in an unbalanced ring that will radiate fast gravity waves. The reason for this is that the size of the ring is too small for the geostrophic balance to be an adequate representation. As De Steur et al. (2004) showed, it is better to prescribe a velocity field such that a *cyclogeostrophic* force balance is obtained. The total force balance is made up of three forces: the horizontal pressure gradient force, the Coriolis force and the centrifugal force. For a circular pressure perturbation this can be written as

$$\frac{V^2}{R} + fV = -\frac{1}{\rho}\frac{\partial p}{\partial n} \tag{3.23}$$

where $V = \sqrt{u^2 + v^2}$ is the total velocity, R is the radial distance from the center of the perturbation and $\frac{\partial p}{\partial n}$ is the outward pressure gradient.

Solving this equation leads to

$$V = -\frac{fR}{2} \pm \sqrt{\frac{f^2R^2}{4} - R\frac{1}{\rho}\frac{\partial p}{\partial n}} \tag{3.24}$$

For a $\frac{\partial p}{\partial n} < 0$ as in the case of a positive pressure perturbation, the pressure gradient can not become larger than $Rf^2/4$ for the velocity to stay real. There are two possible regimes for V (see Holton (1992)). A regular high, with a minus sign, and an anomalous high, with a positive sign of the square root. One has a subgeostrophic velocity field and the other a supergeostrophic, respectively. In this model, the subgeostrophic one has been chosen, as it represents a ring with anticyclonic rotation. The resulting velocity profile is shown in figure 3.6(b).

It turns out that the rings can only be initialized properly when the meridional variation of the Coriolis parameter f is suppressed. On a $\sin(\theta)$-plane, the rings become unstable and radiates gravity waves, hinting at a imbalance. This can be explained by noting that equation (3.23) is only valid for a circlesymmetric system. Using this relation therefor requires that the ring is initialized with a constant f (value taken from the latitude of the maximum sea surface elevation). Directly after initialization, the original $\sin(\theta)$-plane is re-applied. Since this change in f only influences the configuration of the velocity field around the perturbation, and we are to some extent free to choose this, there are no fundamental problems with this approach.

Finally, it should be noted that it is also possible to set a pressure perturbation in the RG-model. This can hardly be called an Agulhas ring, since there is no vertical profile, but it gives physical insight, especially in the processes concerning the radiation of wave energy from the ring.

3.6 Implementation of overturning circulation

The implementation of an overturning circulation is much harder than that of an Agulhas ring. In this research, two approaches have been taken. One uses the pressure at the surface and its motivation comes from a relation found

between the overturning strength and the zonally averaged pressure in the upper layer. The other implementation applies a flux-driven model of the MOC. The motivation of this parameterization lies in a very simple, conceptual, model of the overturning circulation.

3.6.1 Pressure gradient driven circulation

The actual overturning as observed in nature is determined by a delicate interplay of processes like evaporation and atmospheric cooling of the sea surface (see e.g. Weijer et al. (1999)). In general, horizontal density gradients have an effect on the overturning circulation via the pressure gradient. The model at hand does not include a density field, but only two layers of different densities on top of each other. To sustain a horizontal pressure gradient in this model, the sea surface and interface have to be tilted. A transport of water can then come about. But this transport will cancel the tilting of the interface and sea surface, until they are level again. The horizontal pressure gradients have then vanished.

To maintain the horizontal pressure gradients, the model needs some sort of 'engine'. One of the few implementations of overturning circulations in a two layered model in the literature is Andersson and Veronis (2004). The authors use a different mass conservation equation in the governing equations (last equation from (3.1)). Instead of a mass flux changing the layer thickness, the mass flux is used to exchange mass between the layers. In that paper, it is set to a predescribed value, with vertical velocity $w_0(x, y)$. The momentum equations must then follow this w_0. Moreover, the water they remove from the upper layer is inserted in the lower layer (with a density correction ρ_1/ρ_2). With an appropriate choice of $w_0(x, y)$, this is an overturning in the sense that what is removed from the upper layer in the northern part of the domain can be inserted in the lower layer and vice versa in the southern part of the domain.

This model can however not be used in this experiment. Instead of prescribing w_0, it is the goal of this experiment to see how Agulhas rings interact with the Meridional Overturning Circulation. In that sense, w_0 must be an observable instead of a parameter. What we need therefor is a relation between some observable in the model $f(h, u, v)$ and the overturning strength Ψ. In this case

$$f(h, u, v) \propto \Psi = \int w_0 dA \tag{3.25}$$

in which dA is the region where the overturning is applied. Note that the unit of Ψ is $[\mathrm{m}^3/\mathrm{s}]$, as it should be for a transport quantity. Although Ψ will be addressed as the overturning strength, it is formally the North Atlantic Deepwater Formation magnitude.

Off course, w_0 itself can be a function of latitude. In order to avoid discontinuities in the region where the overturning is prescribed (dA) with the rest of

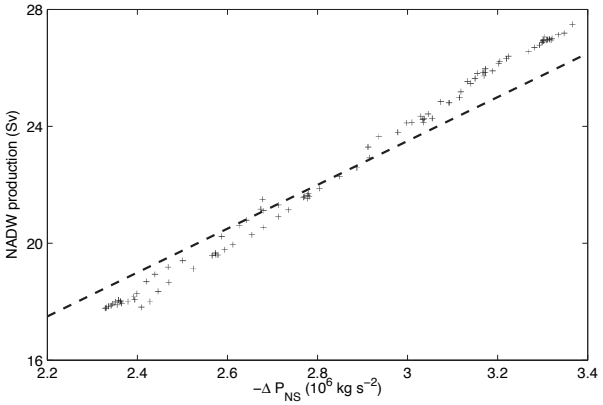

Figure 3.7: The linear relation between the total meridional pressure difference, measured by $\Delta P_{NS} = P_N - P_S = P(53^\circ N) - P(30^\circ S)$ (where $P(\theta) = \int_{-1500}^{0} \tilde{p} dz$ and $\tilde{p}$ the zonally averaged pressure at latitude θ) and the NADW production (maximum overturning strength beyond 30°N) in Sv(=10^6 m^3/s). The picture is taken from Weijer et al. (2002). The dashed line represents the linear fit that has been taken in this thesis (equation (3.29))

the domain, a profile for w_0 has been chosen such that

$$w_0(y) = c \frac{1}{1 + \frac{(y - y_{ref})^2}{\sigma^2}} \tag{3.26}$$

allowing for tuning in the parameter σ. The region of integration dA is zonally uniform and spans the entire domain (length L) and y_{ref} is some reference latitude. Using equation (3.26) in equation (3.25) gives

$$\begin{aligned} \Psi &= \int_0^L \int_{-\Theta}^{\Theta} w_0 d\theta d\phi \\ &= Lc\pi\sigma \qquad \text{if} \quad \Theta \to \infty \end{aligned} \tag{3.27}$$

The meridional domain over which the overturning is applied has to be finite, and a subdomain of the Northern Atlantic. If we choose $\Theta = 125$ km, and require that 95% of the integral in (3.27) has to be covered, we get the result that $\sigma = 10$ km. We are now only left with the constant of proportionality c.

Weijer et al. (1999) already suggest in their two-dimensional model that there is a direct linear dependence between the meridional large-scale pressure difference and the overturning strength. This theoretical result is backed by a later paper (Weijer et al., 2002) in which the authors model the overturning using a large-scale geostrophic model. They find a linear relation between the zonally averaged meridional pressure difference and the overturning strength

(see figure 3.7). The zonally averaged meridional pressure difference is integrated from the sea surface to 1500 m below sea level. The physical explanation of this result is that due to atmospheric heat loss, the density is increased as the water flows northward. This forces a positive pressure difference in the baroclinic pressure field at depth, which causes a southward transport. Due to this southward transport, sea level drops in the northern part of the Atlantic, which causes a negative pressure difference at the sea surface. Although the linearity is not explained, at least not for a 3D-model, we use the result to obtain the desired relation.

The linear relation can be taken as the function f in (3.25). As opposed to the model by Weijer et al. (2002), we cannot integrate to 1500 m depth. It is assumed that the upper branch of the overturning circulation accounts for the upper layer in the model (i.e. the first 500 m). The second layer can then facilitate the return flow of the overturning. With this, we can write for the overturning as a function of the zonally averaged sea surface height $\tilde{\eta}$ (using the hydrostatic equation)

$$\begin{aligned} \Psi = \Psi_0 + c\ \Delta P_{NS} &= \Psi_0 + c \int_{-500}^{0} \left(\int_{-1500}^{\tilde{\eta}_N} \rho_1 g dz - \int_{-1500}^{\tilde{\eta}_S} \rho_1 g dz \right) dz \\ &= \Psi_0 + c\ 500\ \rho_1 g(\tilde{\eta}_N - \tilde{\eta}_S) \end{aligned} \tag{3.28}$$

in which Ψ_0 and c (the same as in equation (3.27)) are the bias and slope which have to be determined from figure 3.7. Determining a best fit from figure 3.7 gives $c \approx -10$ m^{3}s/kg and $\Psi_0 \approx -6$ Sv. These numbers, however, constitute a problem. At zero pressure gradient, the overturning will be negative. This implies upwelling in the Northern Atlantic, something that is not only nonphysical, but also problematic in the context of this model. We would like to start without any pressure difference, and then spin the model up to some equilibrium value for ΔP_{NS} (if there is any). But if the overturning at the start is already negative, there is no hope that the model would reverse by itself. Therefor, we need the constraint that $\Psi_0 > 0$. It has to be chosen whether the fit has to be adjusted (implying a change in c as well as a change in Ψ_0) or that only the bias has to change. Although the choice can be disputed (it is the gradient that is important for our research) the parameters were chosen as

$$\Psi_0 = 1 \text{ Sv} \qquad c = -7.5 \text{ m}^3\text{s/kg} \tag{3.29}$$

This leaves only the latitudes θ_N and θ_S, the latitudes over which to average the pressure, to be determined. This is further addressed in section 4.5.

One could argue that the choice for a nonzero bias Ψ_0 is physically unrealistic. Without any forcing (in this case the meridional pressure gradient), the MOC will probably seize. However, this model requires a nonzero bias. There is no other way that an ocean in rest (without an Agulhas ring) can initiate an overturning circulation. As the research question (page 4) implies that the MOC is already present when the Agulhas ring is released, it is inevitable that

the MOC must be self-starting. The easiest and cleanest way to start it is to prescribe a nonzero bias, which is why this is the procedure we follow.

But apart from this cosmetical problem, the model implementation has a far more problematic drawback. It is absolutely unclear whether the relation found by Weijer et al. (2002) can be used in a simple model like this. Weijer et al. (2002) integrated their pressure over the upper 1500 meters, which in their model is the upper limb of the overturning circulation. In the 11 layer Hamburg LSG model (and many other multi-layered models), the upper 1500 meters encompasses many layers. In our model, however, we have effectively only integrated over the surface elevation (see equation (3.28)). This must be an oversimplification of the dynamics of the system. A better solution would be to integrate over the upper *layer*, but a quick calculation shows that all responses will than increase by a factor 500 (the upper layer thickness is governed by the interface elevation, which is in isostatic equilibrium 500 times the sea surface height). Although the responses may in our configuration be considered small, a 500 times larger response is unphysically large. An Agulhas ring will then account for a 25 Sv change in overturning strength, see also section 4.6. It is therefor clear that it is not useful to integrate over the complete upper layer.

Since the parameterization presented here and motivated by the results of Weijer et al. (2002) is taken from a far more complex model, and it is unclear how this can be used in our model, we will present another parameterization of the overturning: a conceptually motivated one. The results of these different approaches to parameterize the overturning can then be used to test and possibly confirm the legitimacy of the separate approaches.

3.6.2 Flux driven circulation

As was noted in the previous section, the use of a pressure gradient motivated parameterization of the overturning circulation, based on the results from Weijer et al. (2002) has some serious drawbacks, the main being that it is unclear how results from a multilevel global circulation model can be used in a much more simple two-layered one.

A different approach is to return to the conceptual idea of the overturning circulation. If we picture the upper layer as the northward flowing limb of the circulation, and the lower one as the return flow, we can use mass conservation to formulate the overturning: at some latitude, the difference between the inflow through the upper layer and the outflow through the lower layer must be transported from the upper to the lower layer. This transportation then is the overturning circulation, as is depicted in figure 3.8.

In this formulation, it is assumed that all excess water north of a certain latitude will participate in the North Atlantic Deepwater Formation. The model does not give any physical considerations for this and the real ocean water in the upper layer could pile up north of that latitude for some time to be released later as a southward flux. However, support for this idea comes from observationalists since this is exactly the way in which they try to measure the strength of the Meridional Overturning Circulation.

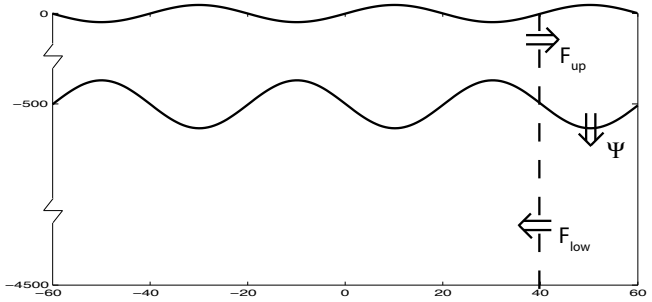

Figure 3.8: A cartoon showing the concept behind the flux driven overturning circulation: The volumetric difference between the inflow in the upper layer F_{up} in the region north of 40°N and the outflow in the lower layer F_{low} will be used for the overturning Ψ.

Note that only baroclinic signals will alter the overturning strength Ψ in this parameterization. A barotropic signal will account for an equal flux in the two layers, yielding a zero flux difference. This is very different from the pressure gradient parameterization, where also barotropic signals can alter the overturning strength as only the sea surface height is concerned. This is therefor one of the great advantages of the flux driven parameterization as it was in the introduction already noted that baroclinic signals are more relevant for changes in the MOC than barotropic ones.

The formulation of the flux driven overturning circulation can be written as:

$$\Psi = \Psi_0 + \frac{1}{2}\left(\int_{\theta_N} v_1 h_1 dx - \int_{\theta_N} v_2 h_2 dx\right) \tag{3.30}$$

with v_1 and v_2 the baroclinic velocities and θ_N some latitude at which the fluxes are calculated. Note that this equation uses the volumetric fluxes, instead of the mass fluxes. Using the boussinesq approximation, however, these are equal.

This equation can be implemented in the same way as the equation based on Weijer et al. (2002) is implemented: using a region in the north of the basin for down-welling and in the south for up-welling with a shape given by equation (3.26). In order to make the two parameterizations better comparable, the bias Ψ_0 will be taken identical to the bias of the previous section (i.e. $\Psi_0 = 1$ Sv).

The latitude over which the fluxes are calculated is still free to choose. This must be far north, as close to the region of mass exchange as possible. On the other hand, there must be some distance between the region of mass exchange and θ_N in order to avoid extreme fluctuations in the overturning strength Ψ. For that reason, the latitude of flux calculation is chosen as

$$\theta_N = 40°\text{N}. \tag{3.31}$$

It must be stressed that this parameterization is highly idealized. By prescribing that the meridional fluxes must balance the overturning, the physical

mechanisms behind the overturning circulation are neglected, even more so than in the Weijer et al. (2002) parameterization.

We now have two parameterizations, equations (3.28) and (3.30). Both will be used in the next chapter, when the model results will be discussed. With these results to back it, the advantages and disadvantages of the two implementations will be discussed after that.

Chapter 4

Results

4.1 The Reduced Gravity model

The first results discussed in this chapter are retrieved from tests that are performed with the Reduced Gravity (RG) model. Section 3.4.1 gives an overview of this model and its implementation. The model is ideal to test whether the transfer from one type of wave to another can be captured in the model runs. This is important since for the model to perform adequately, the conversion from Rossby to Kelvin waves and vice versa must be modelled correctly in this model.

The model has been run for 4000 days (more than 10 years) to simulate the evolution of the Atlantic Ocean. The initially undisturbed interface is disturbed with the model equivalent of an Agulhas ring at day zero.

Figure 4.1 shows the evolution of the perturbation on its way through the Atlantic Ocean. A snapshot of the Sea Surface Height (SSH) has been taken every 300 days, from day number 0 to day 2400. The remaining 1600 days are not depicted, as they show a similar pattern as the last snapshot. If the full ring was to be displayed, the details would be very hard to notice. It is therefor that in this figure (and all the forthcoming) the SSH has been cut of at 1% of the maximum initial perturbation height. Since this perturbation has a maximum height of $\eta_1 = 0.5$ m (see equation (2.2)), this implies a cut-off at 0.005 m. All structures larger than this value are displayed as maximum disturbances. This is the best way to appreciate the fine structure of the ring decay.

It is important to note that since the ring is a positive mass anomaly, the steady state equilibrium SSH will have a height of

$$h_{\text{equilibrium}} =< h >= \frac{M_p}{A_d} = 2.8 \cdot 10^{-4} \text{ m} \tag{4.1}$$

where $M_p = 2.0 \cdot 10^{10}$ m^3 is the total added mass in the perturbation and $A_d = 7.1 \cdot 10^{13}$ m^2 is the area of the ocean basin.

At initiation, day number 0, the ring is positioned at (30°S, 10°E), 1000 km west of the eastern boundary. After initiation, the ring can clearly be seen

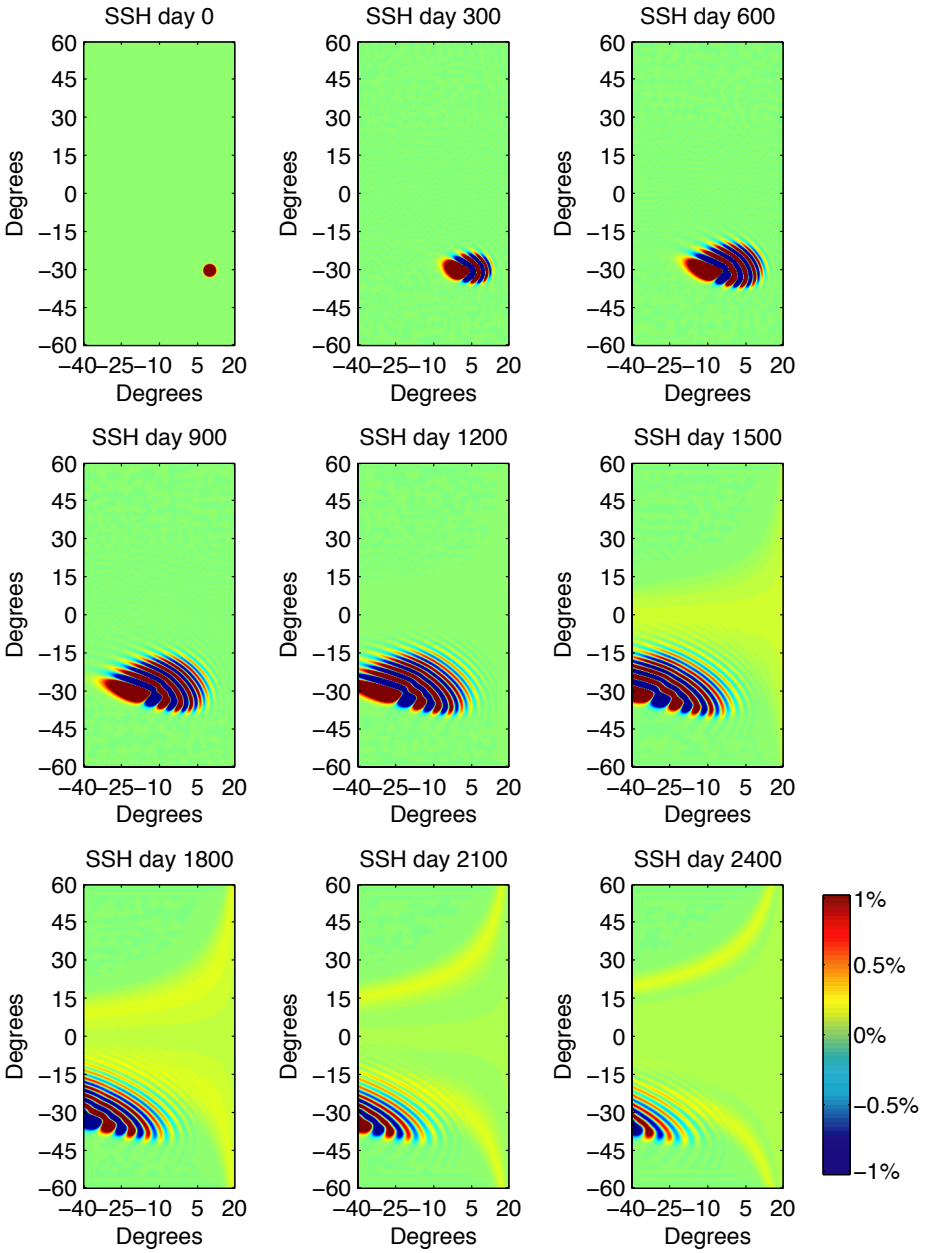

Figure 4.1: 9 Snapshots of the Sea Surface Height (SSH) of the Reduced Gravity model, after 0, 300, 600, 900, 1200, 1500, 1800, 2100 and 2400 days respectively. The scale runs from -1% to $+1\%$ of the initial (positive) perturbation height (0.5 m). The first picture shows the initial perturbation, the next four the Rossby waves radiated as the perturbation crosses the Atlantic. The fifth picture shows the Kelvin wave across the equator, and the last four pictures show the basin-mode Rossby wave.

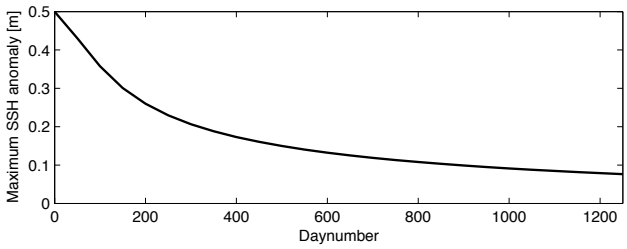

Figure 4.2: The decay of the Agulhas ring. The maximum Sea Surface Height (SSH) is plotted against the time.

travelling across the Atlantic Ocean to the western boundary. Due to the cyclo-geostrophic balance and nonlinear interactions, the ring stays remarkably intact on its journey. There are a number of processes that take place in this period:

- The ring moves westward.
- The sea surface at the location where the ring was initialized keeps oscillating and thereby radiates more Rossby waves. These waves follow the ring as tail-waves.
- The tail-waves curve around the ring on the north side, but not on its south side.
- The ring and tail-waves tilt towards the northwest.

At first sight, it seems that the ring behaves like a Rossby wave. As the wave is relatively long, it can only travel westward in the way that has been described in section 2.4. From the figures, it follows that the perturbation moves $50°(= 5000$ km) in 1500 days. This constitutes an approximate phase speed of $c = 3.8$ cm/s. A more detailed study, focussing at the displacement of the maximum elevation (top of the perturbation) with time, confirms this phase speed of

$$c = 3.78 \text{ cm/s} \tag{4.2}$$

As was discussed in section 2.4, the theoretical phase speed of the fastest (longest) Rossby wave at 30°S is

$$c = \beta R_d^2 = \beta \frac{gH}{f^2} = 3.67 \text{ cm/s} \tag{4.3}$$

The difference between (4.2) and (4.3) is small. We can conclude that the model is well capable in resembling the Rossby waves.

Figure 4.2 shows the maximum SSH as a function of time. The decaying of the ring can clearly be followed. Initially, the decay is rapid and linear with time. After approximately 150 days, the decaying slows down. This is in good agreement with what Schouten et al. (2000) find on the decaying of Agulhas rings in nature. The difference is that in this model the ring keeps decaying

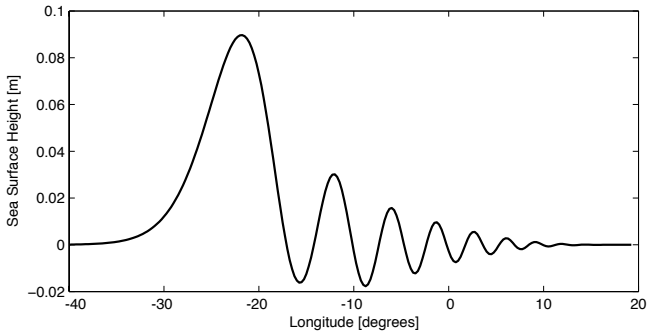

Figure 4.3: The Sea Surface Height (SSH) after 1000 days of iteration of the RG-model. The figure shows a cross-section along 30° S.

whereas in nature the rings stop decaying after 300 days. This might be related to the fact that real Agulhas rings encounter the Walvis Ridge and such a ridge tends to tamper Rossby wave radiation, leading to a smaller decay (De Steur, 2005).

Figure 4.3 shows a cross-section through the sea surface at day number 1000. The perturbation has almost completely crossed the Southern Atlantic, and has a very regular shape. Its wavelength is 500 km, as can be deducted from the zero-crossings of this figure. Further note that the maximum SSH has decreased from an initial 50 cm to merely 9.0 cm.

When returning to the nine snapshots of figure 4.1, the tilting of the tail-waves can be understood from the variation of the phase speed of plane Rossby waves with latitude. As the tail-waves curl around the perturbation, the northward extensions of the wave move faster than the southward. Moreover, no Rossby waves from the ring can be observed south of 40°S. This is due to the forcing frequency, which is beyond 40°S larger than the maximum frequency of free plane Rossby waves. This maximum is given by

$$\omega_{\max} = \frac{\beta R_d}{2} \tag{4.4}$$

which at 40°S is $2.9 \cdot 10^{-7}$ s^{-1}. The forcing frequency, deducted from the figures 4.1 and 4.3 (where $\omega = \frac{2\pi c}{\lambda}$, with λ the wave length) is $3.0 \cdot 10^{-7}$ s^{-1}, which is indeed larger than the maximum frequency of free plane Rossby waves.

After the ring has reached the western boundary of the domain, the Rossby wave energy is transformed into Kelvin wave energy. The resulting Kelvin wave must have a northward group velocity for the balance in figure 2.1 to be fulfilled. Liu et al. (1999) discusses the transformation from Kelvin to Rossby waves and vice versa. They argue that as the forcing frequency vanishes, so does the wave-number. And with a small wave-number, the Kelvin wave can become a Kelvin current, transporting mass away from the perturbation. It is hardly possible to see the Kelvin wave actually travel along the western boundary, but as it hits the equator, it can clearly be seen by the rise of the equatorial sea surface.

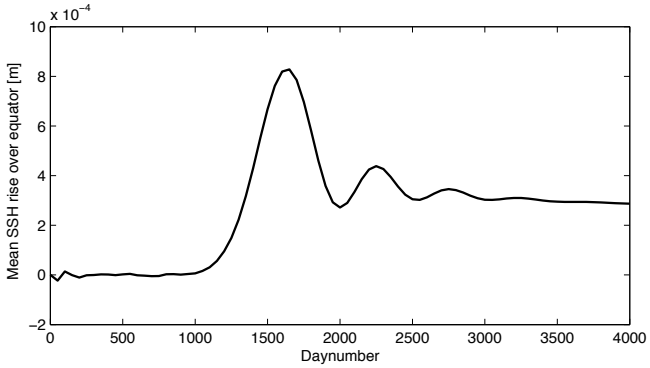

Figure 4.4: The equatorial mean SSH *as a function of time. After day 1000, the Kelvin wave starts to build up, reaching a maximum at day 1700. After that, the largest part of the perturbation has passed the equator and the interface elevation settles at the equilibrium height from equation* (4.1).

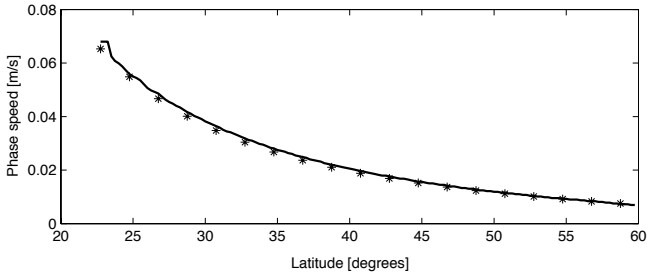

Figure 4.5: The phase speed of the basin mode Rossby wave in the Northern Atlantic. Results from the model (solid line) and theoretical calculations (stars) are depicted.

Figure 4.4 shows the mean SSH at the equator over time. After 1000 days, the sea surface starts to rise slowly. This is the moment at which the equatorial Kelvin current is formed, and the excess water can flow eastward. 1800 Days after initiation, most of the water has been transported to the eastern boundary, and the SSH slowly starts to drop to a height of 0.3 mm, the equilibrium height from equation (4.1).

As the Kelvin current flows both north- and southward along the eastern border, it radiates a Rossby wave. Because of the dependence of the phase speed on latitude, the wave moves slower as the distance from the equator increases. Figure 4.5 shows the phase speed of the Rossby wave as it travels westward. This is in good agreement with the theoretical phase speed for linear plane Rossby waves (stars in the picture). The transition from an equatorial Kelvin wave through eastern boundary Kelvin waves and Rossby waves is similar to what Anderson and Rowlands (1976) find in their study on the incidence of an equatorial Kelvin wave on a meridional boundary.

The plots already give an estimate of the response time of the MOC on an Agulhas Ring. It takes approximately 1500 days (4 years) for the ring signal to reach the northern part of the basin as a Kelvin wave.

These results provide a firm fundament for further research. We have shown that a simple RG-model is capable of modelling the kind of complex physics that is needed to answer the research questions. This model is already capable of moving mass from the South Atlantic to the North Atlantic Ocean. The entire process takes about 7–10 years. Most of that time is used by the Southern Atlantic initial Rossby wave to travel to the western boundary (approximately 1500 days) and by the North Atlantic basin mode to travel from the eastern boundary into the basin (approximately 2000 days). The model run therefor provides us with an upper bound for the response time. We can now investigate faster responses, including the barotropic mode of the ocean. For that, a Two Layer model is required.

4.2 Near-coastal solutions

However, before discussing the Two Layer model and the barotropic mode of the Agulhas ring, it is worthwhile to further investigate some of the features of the RG-model. As already discussed in section 1.2, Johnson and Marshall (2002b) describe an experiment in which a perturbation is released at the western boundary. In their RG-model, the perturbation is released at 60°N mimicking the Meridional Overturning Circulation. Their final result is comparable to the result discussed in the previous section, without the first 1500 days of the perturbation travelling westward. An interesting results is that they can in much more detail see the Kelvin wave cross the equator and travel pole-ward along the eastern boundary. This is behavior that has not been observed in the RG-model run of the previous section. It is therefor interesting to see whether their results are reproducible by our RG-model.

As we want to stay close to the research question (page 4), some adjustments compared to the experiment of Johnson and Marshall (2002b) have been made. The perturbation is moved to (30°S, 37.5°W). Moreover, in comparison to the original experiment by Johnson and Marshall (2002b), the southern border sponge region has been left out.

The distance from the western coast is too small for the perturbation to be in cyclogeostrophic balance. We can therefor expect for the perturbation to radiate gravity waves. Nine snapshots of the perturbation are shown in figure 4.6. Despite the large amount of gravity-inertial wave noise, the results provide a good anatomy of the mechanisms governing the mass transport. After 10 days, the Kelvin wave emerging from the perturbation has reached the equator. At that moment, a current transports mass along the equator to the east. This takes approximately 20 days. After that, the current moves pole-ward, as the snapshot of day 40 clearly shows. The snapshots also show that the only mass transport on the western boundary is equator-ward as is expected from Kelvin wave theory. An estimation from the snapshots for the phase speed of the

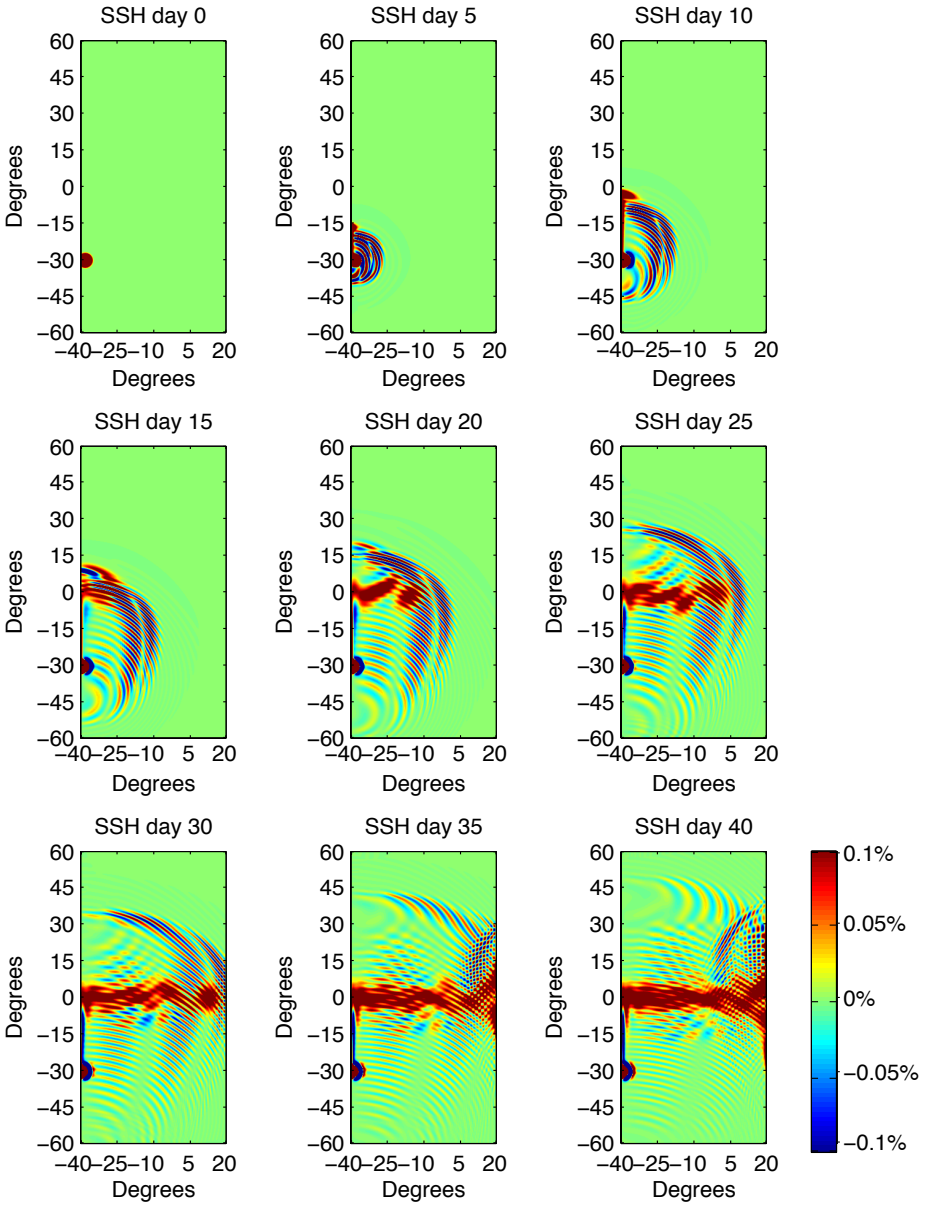

Figure 4.6: 9 Snapshots of the Interface Elevation (IE) *of the Reduced Gravity model, after 0, 5, 10, 15, 20, 25, 30, 35 and 40 days respectively. The scale runs from* -0.1% *to* $+0.1\%$ *of the initial (positive) perturbation height* (0.5 m).

equatorial Kelvin wave is

$$c = \frac{6 \cdot 10^6 \text{ m}}{20 \text{ days}} = 3.5 \text{ m/s} \tag{4.5}$$

whereas the theoretical phase speed of a Kelvin wave is

$$c = \sqrt{g'H} = 3.1 \text{ m/s} \tag{4.6}$$

These two numbers are again in good agreement, especially since the estimation of the phase speed from the snapshots is relatively difficult.

Although the large-scale experiment of the first section did not show the emerging Kelvin wave, these snapshots provide evidence that the model is capable of mimicking such an equatorial wave as a horizontally moving structure. One possible reason for the absence of this wavefront in the large experiment is that the structure of the perturbation on the western boundary is very different from the structure in this experiment. In the previous experiment, the SSH slowly rises as the perturbation arrives as the coast, since the horizontal scale is large. Therefor, the equatorial Kelvin wave also starts with a very low SSH. As the perturbation reaches the coast, more and more water is transported along the equator. But the initial Kelvin wave, which behaves as a current, has then already been set up. The only quantity that varies is the amount of mass transport.

We can conclude that the model is capable of reproducing the results presented by Johnson and Marshall (2002b). The experiment has been a good test for the model robustness, since a ring close to the coast is relatively unstable.

4.3 The Two Layer model

Now that the Reduced Gravity model has fully been investigated (with promising results), it is time to look at the Two Layer (TL) model. The Agulhas ring can now be implemented as described in section 3.5.

Integrating the model for 2400 days (≈ 6.5 years) yields a sea surface height and interface elevation as shown in figures 4.7 and 4.8 respectively. The interface elevation is still similar to that of the reduced gravity model, figure 4.1 (note that the colors at the interface are reversed as the ring resembles a negative interface elevation). The most eminent difference is that in the TL-model the Agulhas ring is not as stable as it was in the RG-model. This is due to the larger Rossby deformation radius of the barotropic mode. The scale of the ring is small compared to the barotropic R_d (equation (3.8)) and this alters the dynamics of the ring.

The snapshots of the sea surface height (SSH) show much more noise. Although the slowly travelling ring is still clearly visible, the snapshots also reveal structure in the area where the influence of the ring was not present in the interface elevation. As the Rossby deformation radius R_d is larger, the Agulhas ring itself is not a large-scale perturbation anymore. Instead, short eastward

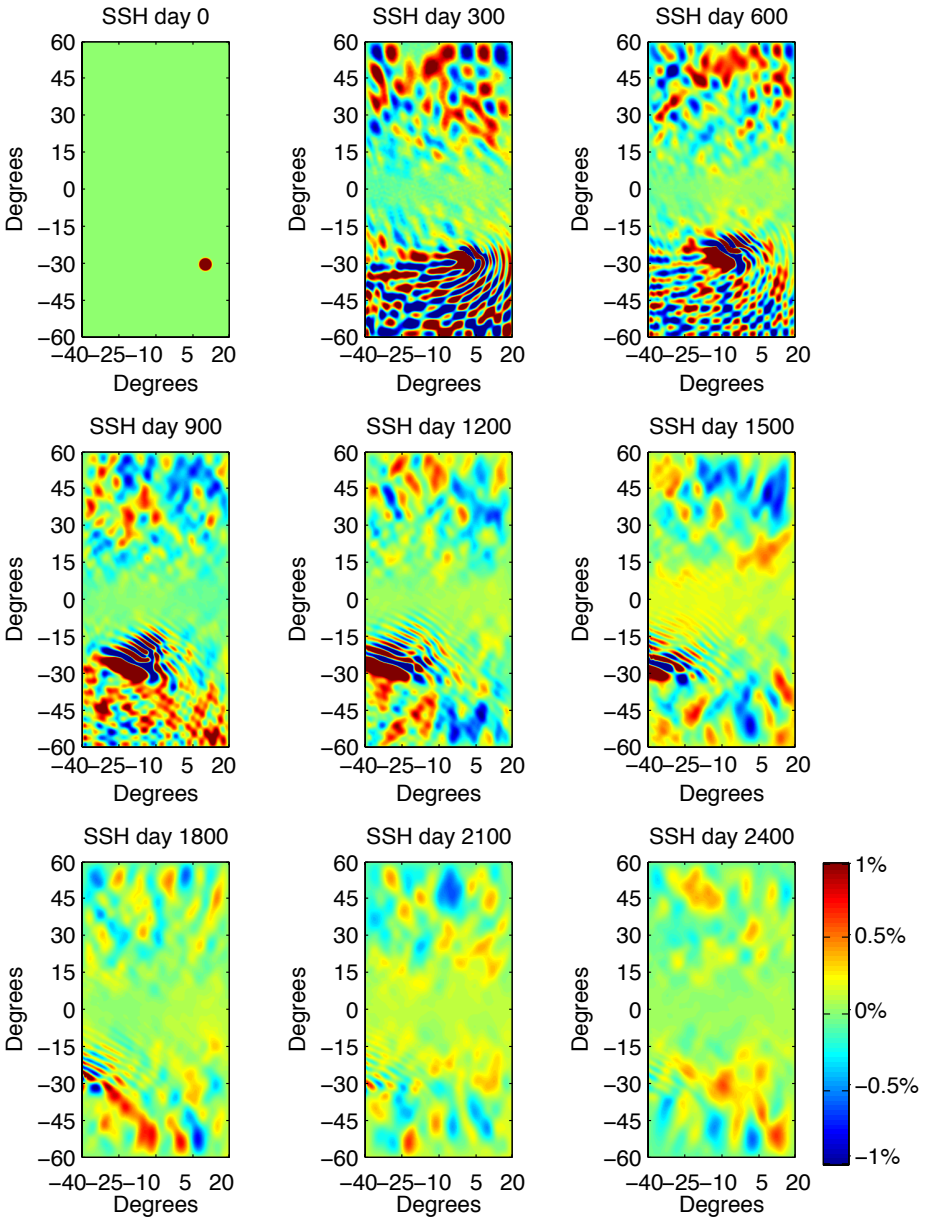

Figure 4.7: 9 Snapshots of the Sea Surface Height (SSH) of the Two Layer model. The scale runs from -1% to $+1\%$ of the initial (positive) perturbation height (0.5 m). Figure 4.8 shows the corresponding Interface Elevation.

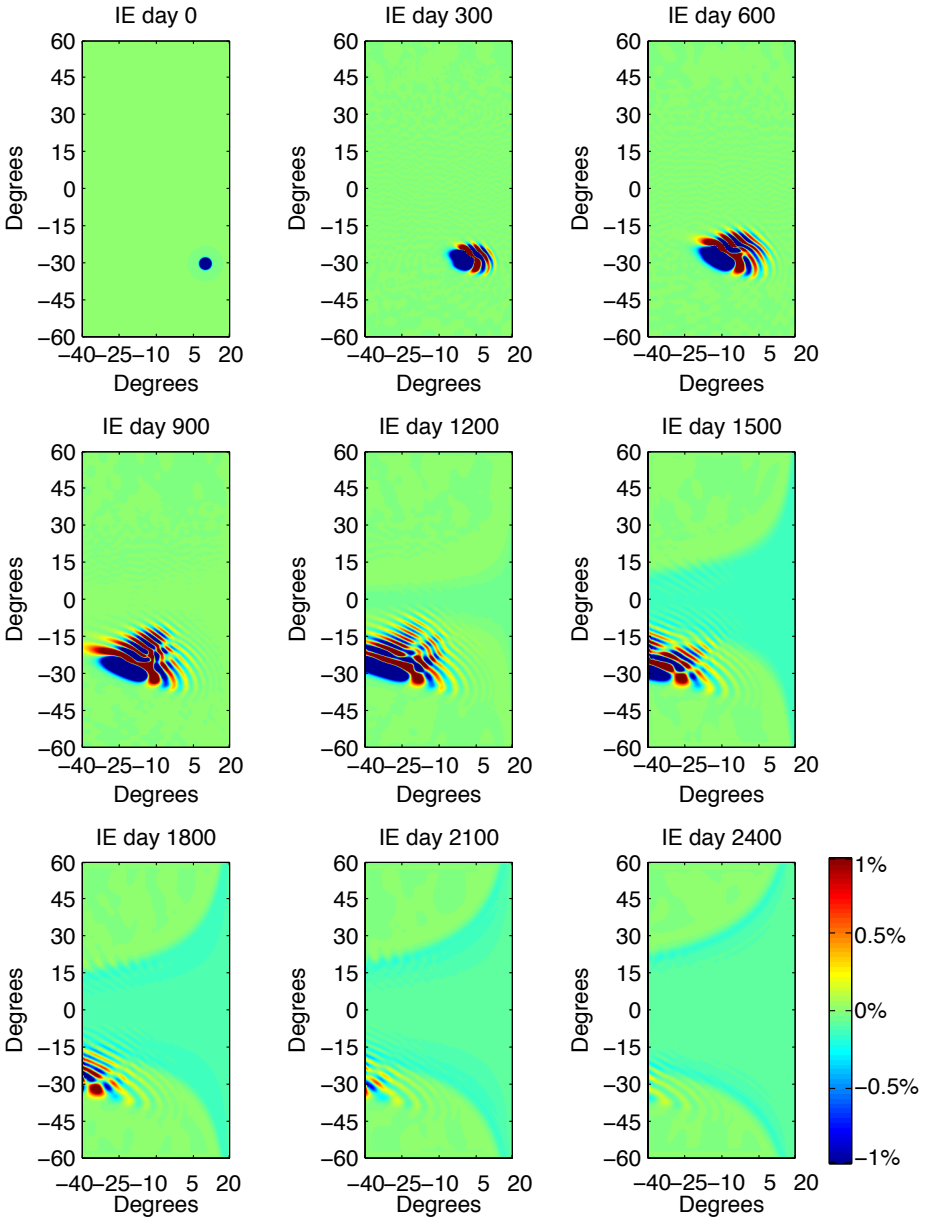

*Figure 4.8: 9 Snapshots of the Interface Elevation (*IE*) of the Two Layer model. The scale runs from −1% to +1% of the initial (negative) perturbation height (*200 m*). Figure 4.7 shows the corresponding Sea Surface Height.*

travelling Rossby waves are triggered. The waves can be identified as Rossby waves since their phase speed is what can be expected for Rossby waves (not shown). These short waves form an intricate pattern on the sea surface, both on the northern and southern hemisphere. Near the equator, the Rossby waves seem to be absent.

The plots show that the time scale for the baroclinic signal to reach the northern part of the basin is approximately 1500 days, as it was in the RG-model. Weijer et al. (2002) find a response time of 6 years and argue that this is an order of magnitude too large due to their large resolution. Our results however, are in much better agreement with what they find than this factor 10.

The time scale of the barotropic signal is much smaller than 300 days, since after 300 days signals can already be seen in the entire basin of figure 4.7. Longuet-Higgins (1965) shows that the envelope of the barotropic signal of a localized disturbance spreads throughout the basin with a velocity of approximately βR_d^2. In our case this is in the order of 100 m/s. It seems that the Agulhas ring cannot be analyzed by using linear *plane* Rossby waves. While this theory predicts that these short Rossby waves have an eastward group velocity, we can clearly see (especially in the SSH snapshot of day 300) that the short Rossby waves transport their energy also westward.

The fact that linear theory breaks down, is also present in the phase speed of the baroclinic mode. In the Rossby wave stage, the ring travels faster than it did in the RG-model run. As already shown in section 2.4, the baroclinic Rossby wave dispersion relation of a two-layer system is

$$\omega = \frac{-\beta l}{l^2 + m^2 + \frac{f^2}{g' h_1} + \frac{f^2}{g' h_2}} \tag{4.7}$$

with h_1 and h_2 the layer thicknesses of the upper and lower layer respectively. The phase speed for long waves is therefor

$$c = -\beta \frac{g'}{f^2} \frac{h_1 h_2}{h_1 + h_2} \tag{4.8}$$

which is a factor $\frac{h_2}{h_1+h_2}$ smaller than the phase speed for Rossby waves in the RG-model. Deriving the phase speed of the perturbation from the model movement of the Agulhas ring, however, yields a phase speed that is *larger* than that of the RG-model. In this case, it is (ref. equation (4.2))

$$c = 4.3 \text{ cm/s} \tag{4.9}$$

While the theory predicts a decrease in phase speed of 12%, the model gives an increase of 13%. We must conclude that the dynamics of the ring in this respect can not be approximated by linear Rossby wave dynamics.

4.4 The Mid-Atlantic Ridge

In the third research question it is argued whether the presence of a topographic ridge can reduce the time it takes for an Agulhas ring to influence the Meridional

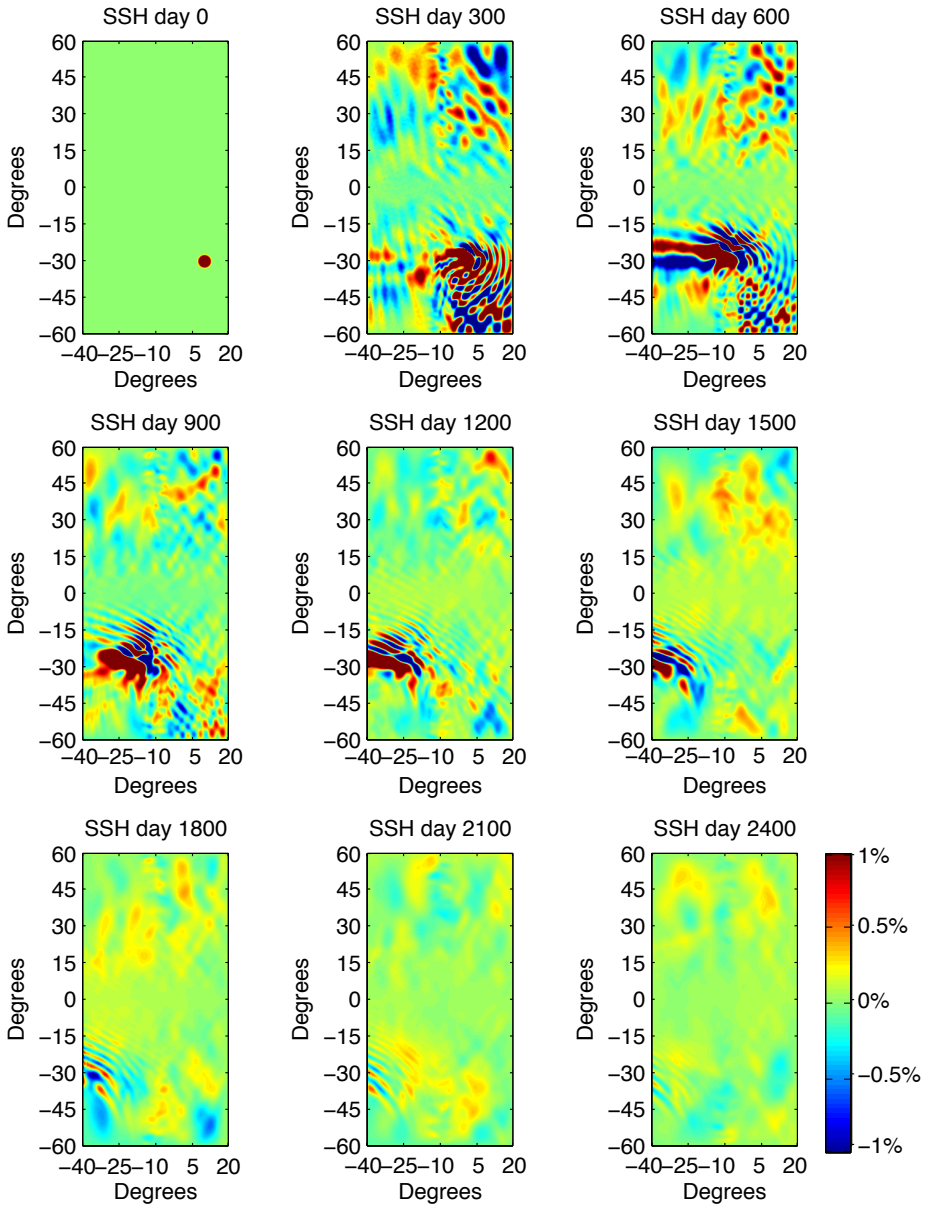

Figure 4.9: 9 Snapshots of the Sea Surface Height (SSH) of the Two Layer model including a Mid-Atlantic Ridge. The scale runs from −1% to +1% of the initial (positive) perturbation height (0.5 m). Figure 4.10 shows the corresponding Interface Elevation.

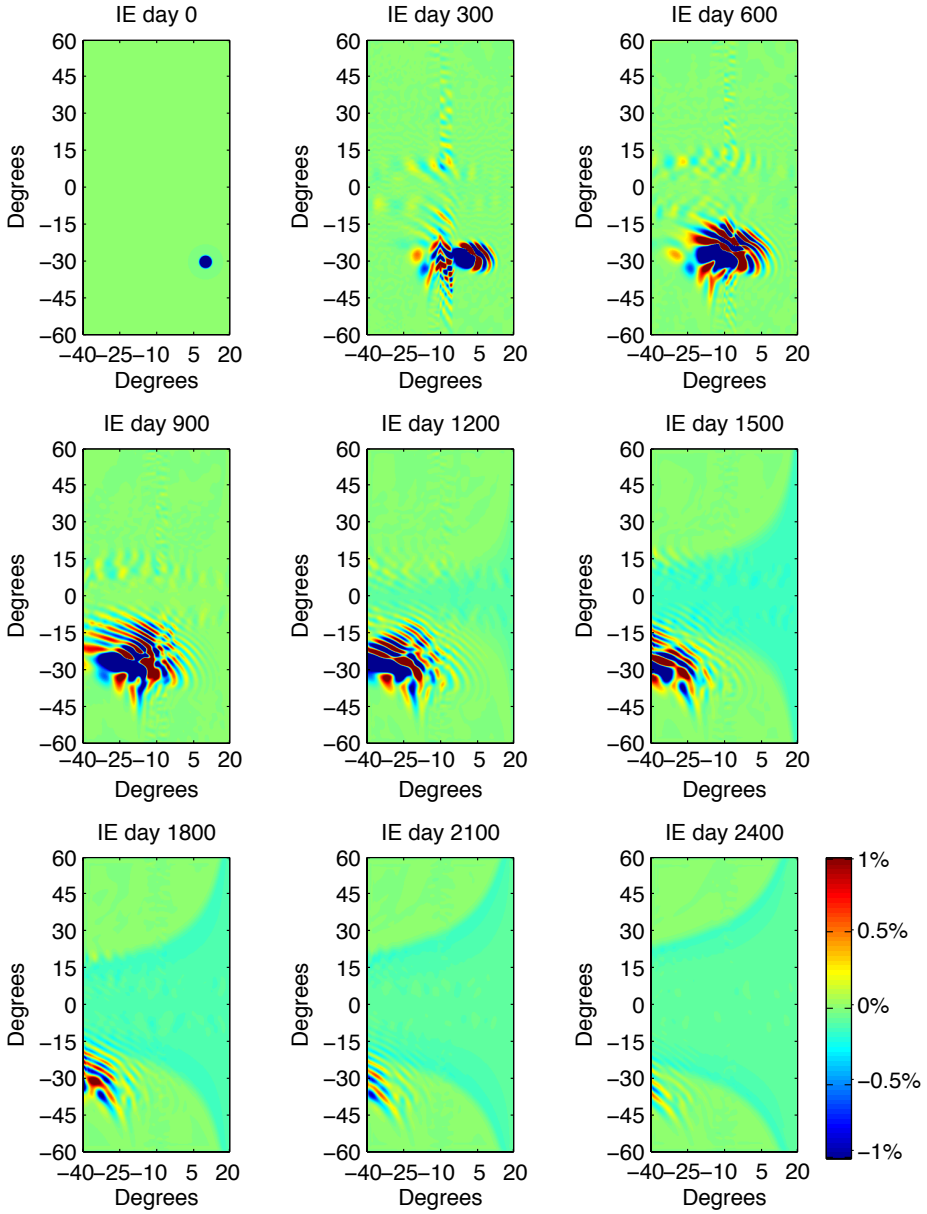

*Figure 4.10: 9 Snapshots of the Interface Elevation (*IE*) of the Two Layer model including a Mid-Atlantic Ridge. The scale runs from* -1% *to* $+1\%$ *of the initial (negative) perturbation height* (200 m)*. Figure 4.9 shows the corresponding Sea Surface Height.*

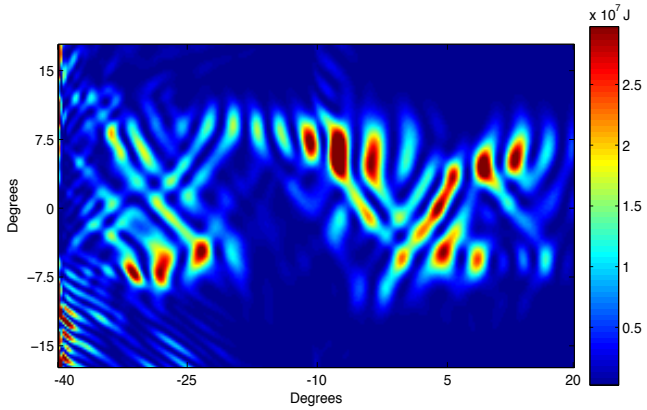

Figure 4.11: The baroclinic energy after 2500 days in the TL*-model including a* MAR*. The figure shows a part of the total domain, the equatorial zone. There is a clear manifestation of a waveguide (c.f. Gill (1982, p. 441))*

Overturning Circulation. To investigate this, a highly idealized Mid-Atlantic Ridge (MAR) has been placed in the middle of the basin. The geometrical configuration of the ridge can be seen in figure 3.1. The model has been rerun using the same parameters as in the TL-experiment. Figures 4.9 and 4.10 show nine snapshots of the sea surface height and interface elevation respectively.

Comparing these figures with the figures of the two-layer model (4.7 and 4.8), there are evident changes when the MAR is included in the model. At the sea surface, the small barotropic waves are confined to the eastern half of the basin. As these waves extend throughout the entire water column, they cannot pass the MAR and are largely trapped in the eastern half of the ocean, where they are generated.

The Agulhas ring itself is completely deformed as it passes the MAR. Especially the snapshot of day 600 shows an interesting phenomenon. As the ring passes over the MAR, a number of zonal rays form between the ring and the western coast. These rays have alternatively high and low SSH and, via geostrophy, transport mass very quickly between the MAR and the western coast. It is unclear how these rays are generated, but they are formed at the moment the ring center passes the summit of the MAR. 200 Days later, when the ring center has passed the MAR to return on level ocean floor, the rays vanish again.

In the interface elevation snapshots, the ring has completely deformed as it has passed the MAR. Moreover, there is baroclinic energy present along the ridge all the way to the northern part of the basin. The response time might therefor be reduced to less than 300 days. However, the amount of baroclinic energy that is bounded to the ridge is very small. If we want to study the possibly decreased response time, we will have to focus on the energy to find out if the response is significant.

First, however, there is a very interesting feature that comes out of the

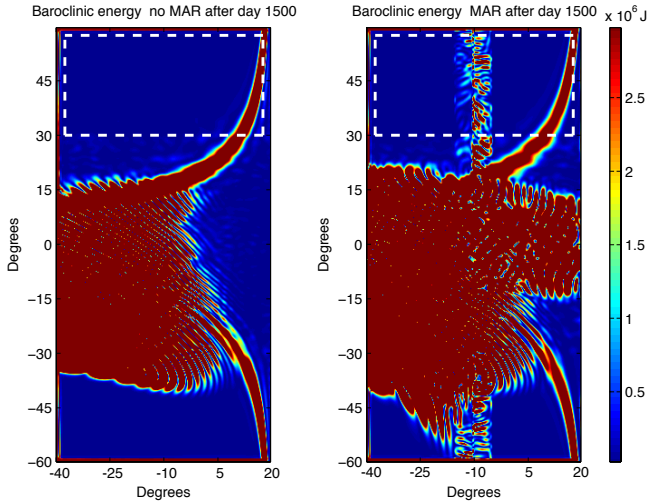

Figure 4.12: The baroclinic energy after 1500 days in the TL*-model without (left) and with (right) a* MAR*. The scale runs from* 0 *to* 3 MJ*. The occurrence of both the equatorial wave-guide and topographic Rossby waves can clearly be seen in the right figure. These phenomena are absent in the left one.*

snapshots of the implementation of a MAR. Figure 4.11 shows a close-up of the baroclinic energy around the equator at the end of the model run. It reveals the manifestation of a wave-guide, an equatorial phenomenon. Inertial gravity waves which are generated near the equator can have a meridional velocity component, but as the factor β/f decreases when the distance from the equator increases, the meridional velocity becomes zero. At this critical latitude, or 'turning point', the wave energy is reflected back to the equator. Following Gill (1982), the relation for the critical latitude θ_c of the equatorial waveguide is

$$f(\theta_c)^2 = (2n+1)c\beta(\theta_c) \tag{4.10}$$

where $n = 2$ is the number of the baroclinic mode and c the gravity wave phase velocity $\sqrt{g'h_1} = 4.3$ m/s. This equation can be solved when $f = 2\Omega \sin\theta$ and $\beta = \frac{2\Omega}{r}\cos\theta$, leading to

$$\theta_c = 9.6^\circ \tag{4.11}$$

which is in good agreement with the turning latitude that can be deduced from figure 4.11.

It is interesting that the wave-guide does not show up in the TL-model without a MAR. Theoretically, the MAR does not influence relation (4.10). As figure 4.12, which is a snapshot of the baroclinic energy (calculated using equation (2.24)) at day 1500, shows, the amount of energy brought into the equatorial zone is not lower for the MAR-experiment in comparison with the TL-experiment. A possible lack of energy to sustain the equatorial waveguide can therefor not be the explanation of the absence of this phenomena in the TL-experiment.

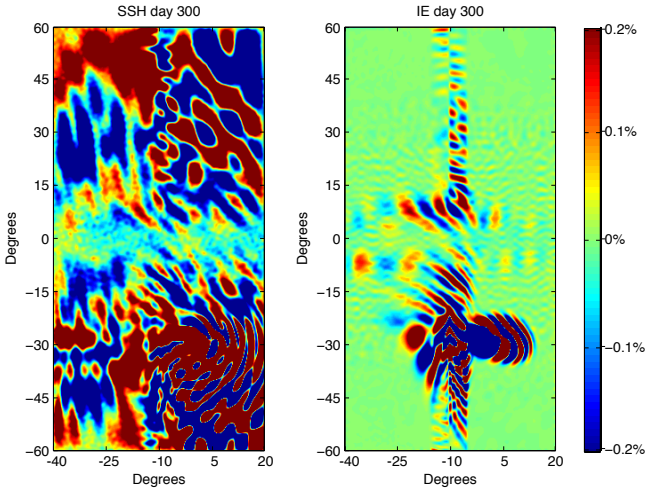

Figure 4.13: The SSH *and* IE *after 300 days for the model with a* MAR. *The scale has been adjusted in comparison with other plots, to focus on the low-amplitude topographic Rossby waves.*

Another explanation is that the required equatorial inertial gravity waves are only forced on a topographic ridge. However, due to the complex wave pattern in the model results, it is very difficult to test whether this statement is true.

A phenomenon that is better understood is the occurrence of topographic Rossby waves that can already be seen in figure 4.12 but is more evident in figure 4.13. After 300 days, as the Agulhas ring hits the MAR, topographic Rossby waves are triggered. In view of the discussion in section 2.5, these waves can be well-understood. The ring hits the eastern side of the MAR, and therefor the righthand plot of figure 2.3 is valid. Moreover, we can see that the zonal extent of the topographic Rossby wave is equal to the width of the slope, 500 km, just as the validation of the theoretical plot, figure 2.3, requires. As the ring collides with the ridge at 30°S, it will generate waves. If the wave length is larger than 200 km, it will move northward to the equator, otherwise it will travel in the direction of the South Pole. This can be seen in the interface elevation of figure 4.13. Although it is not very clear, the waves south of 30°S do have smaller meridional wavelength than those north. For the waves that travel north, the ones with positive wavenumber l experience a change of sign in the group velocity at approximately 10°S. Around this latitude, the topographic waves come loose from the MAR and start to travel both east and westward as normal Rossby waves.

At the equator itself, the amplitude of the waves drops, both in the SSH and in the IE. This effect on the amplitude of Rossby waves in the equatorial region was already noted in the discussion of the TL-experiment. In the northern hemisphere, the waves travel southward on the eastern side of the ridge. The energy is brought to this hemisphere by the barotropic waves, which travel much

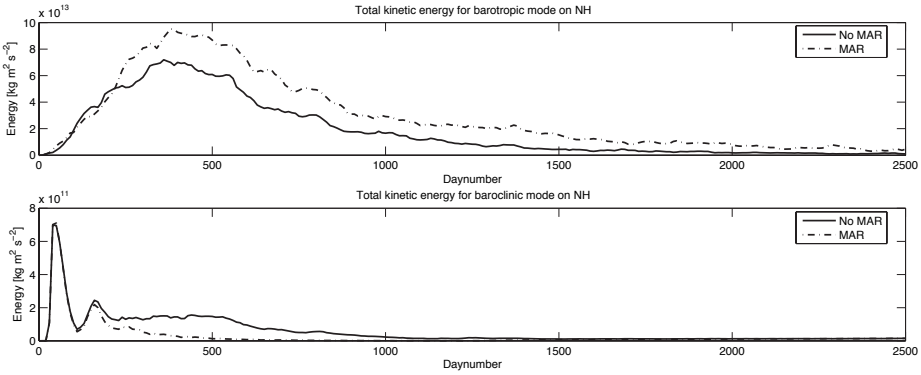

Figure 4.14: The barotropic (upper) and baroclinic (lower) energy in the northern hemisphere (boxed dashed area in figure 4.12) as a function of time. Note the difference in vertical scales; the baroclinic energy is a factor 100 smaller than the barotropic. The figures show the energies for the runs without a MAR *(solid) and with a* MAR *(dash-dotted).*

faster and cannot cross the ridge, as the SSH of figure 4.13 clearly shows.

The figure also reveals that what was expected does not happen. As the barotropic waves on the northern hemisphere collide with the MAR, they do not transform to baroclinic waves which then travel westward and thereby alter the Meridional Overturning Circulation. Instead, the energy is transported in the direction of the equator and released at 10°N, far too southward to influence the MOC.

In order to further investigate this, the barotropic and baroclinic energy have been plotted against time. The energy is integrated over the area boxed by the dashed line in figure 4.12. This region is the domain from 30°N to 60°N without the areas close to the boundaries. This is done as not to include the energy of Kelvin waves travelling along the coasts of the northern hemisphere.

To calculate the barotropic and baroclinic energy, equations (2.23) and (2.24) have been used. The results are plotted in figure 4.14. Note the large difference in the scale of the energies. The high peaks in the baroclinic energy after 100 and 200 days are due to the gravity waves that are radiated from the ring at initiation. These waves are radiated northward before being reflected at 40°N southward (not shown). At 40°S, the waves are reflected again to travel northward. This explains the second (less pronounced) peak. Although this effect is very small, due to the cyclogeostrophic balance, it is by far the most important effect in the baroclinic energy.

Apparently, the barotropic energy level on the northern hemisphere is enhanced by the presence of a MAR. There is no evidence of an enhancement of baroclinic energy in the northern hemisphere when a MAR is included in the model geometry. Instead, we can in general say that the level of kinetic energy is extremely low, suggesting that Agulhas rings do not influence the barotropic

and baroclinic energy at all. This must then be due to very low velocities, as the layer thicknesses are actually altered by the Agulhas ring.

The time scale of the barotropic signals to travel to the northernmost part of the basin have not been altered when the MAR is included in the model geometry. The baroclinic signal does travel much faster to the northern part of the basin. Within 300 days, the baroclinic energy has radiated along the ridge. However, the amount of energy that is affiliated with these topographic Rossby waves is very small. It is therefor doubtful whether the MOC will be influenced by the presence of a MAR. To test this, and to attempt to quantify the responses, a MOC will now be integrated into the model.

4.5 The Meridional Overturning Circulation

As was already discussed in section 3.6, two ways to implement the Meridional Overturning Circulation have been proposed. One is based on the sea surface pressure gradient and the other on the inter-layer volumetric flux difference. The spin-up and steady state (i.e. the dynamics without the introduction of an Agulhas Ring) of both implementations will now be discussed.

4.5.1 Pressure gradient driven circulation

In this experiment, the Meridional Overturning Circulation (MOC) is implemented in the way discussed in section 3.6.1. As was already noticed there, the choice of the two latitudes over which to compute the zonally averaged pressure is still free. It is logical to start with latitudes close to those of Weijer et al. (2002). The authors in that paper use $\theta_N = 53°\text{N}$ as the latitude over which to calculate P_N and $\theta_S = 30°\text{S}$ for the calculation of P_S. However, the Agulhas ring is also released at $\theta = 30°\text{S}$ and this can drastically change P_S at the moment the ring is initiated as the accompanying sea surface rise will alter the zonally averaged pressure in a sudden and unrealistic manner. In order to avoid problems, the southern latitude is therefor shifted northward to 10°S, far away from any immediate direct effect.

Figure 4.15 shows the evolution with time of the overturning Ψ as computed from equation 3.28. At initiation, the overturning is $\Psi_0 = 1$ Sv and for the first 800 days this does not change notably. After this period of little change, pressure at θ_S and θ_N starts to vary and with it the MOC. First the overturning strength drops to a minimum of 0.6 Sv at day 3200, after which it rises again to the initial value of 1 SV.

The figure also shows the meridional transport over the equator. It starts at zero and after 3000 days resembles the inter-layer transport by the MOC. It makes sense that, to first order, all mass that is overturned must pass the equator. The transport and overturning therefor have to be of the same order, as the figure confirms. At the day that overturning and transport are equal, the spin-up has completed, and we can say that the overturning has reached a steady state, although fluctuations are still present.

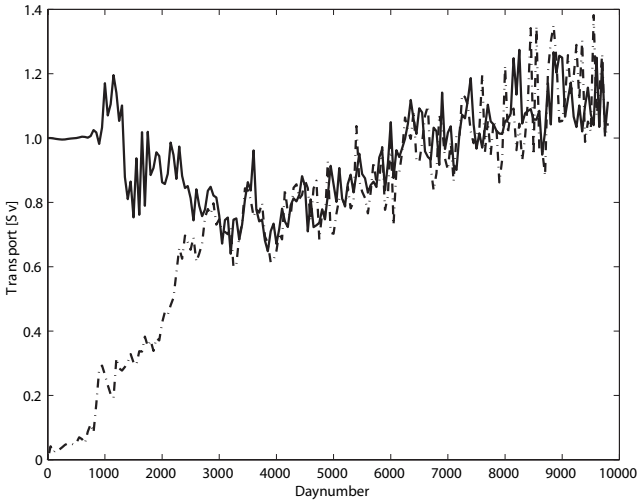

Figure 4.15: The overturning strength Ψ (solid) and transport over the equator (dash-dotted) as a function of day number for the experiment where $\theta_N = 53°N$ and $\theta_S = 10°S$.

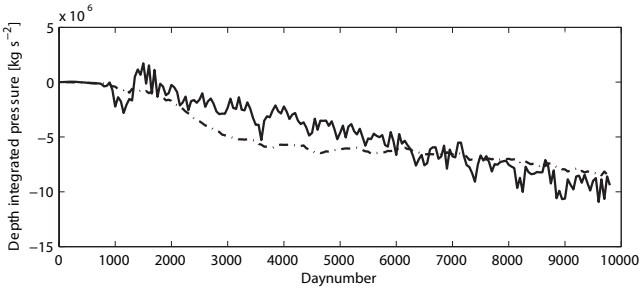

Figure 4.16: The components P_N (solid) and P_S (dash-dotted) for the overturning strength as in figure 4.15

Since θ_N is closer to the region where the vertical transport occurs, changes in P_N will first show up in the plot. This conceptual picture has evidence in figure 4.16, where the separate values for P_N and P_S are computed. This figure also shows that the noisy signal of Ψ is mainly due to high frequency variations in P_N, and not so much in P_S.

The high variability at high frequencies can be suppressed by using the average over a 10° wide domain. This is shown in figure 4.17. Instead of using $\theta_N = 53°$N, an average over the domain (40–50)°N has been taken. This average removes all the fast fluctuations that are present in figure 4.16. To be complete, the same procedure was followed on the southern hemisphere, where two possible domains were investigated. The overturning strength is not influenced by the

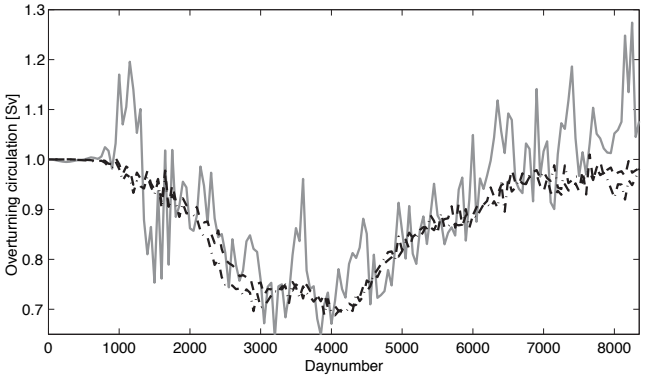

Figure 4.17: The overturning strength Ψ for different configurations of θ_N and θ_S (see table 4.1): A (solid, gray), B (dash-dotted) and C (dashed)

exact location of the southern domain (see figure 4.17). However, the location must be such that an Agulhas ring is not placed inside the domain. The location of the domain in the northern hemisphere has been placed as far northward as possible, without obstructing the region of downwelling.

We will perform experiments with three different configurations of the location of θ_N and θ_S. These three configurations, named A, B and C are summarized in table 4.1.

Figure 4.18 shows a snapshot of the SSH and the IE after 2500 days. This is still in the spin up period of the overturning, but the figure already reveals how the actual overturning is realized. In the top northern and southern regions, the elevation is extremely high or low. While the figure shows a cut-off at 2 m for the interface, the maximum height in these regions for the interface elevation is 140 m. These are the regions where the layer thickness is adjusted, and the regions are exact opposites of each other with respect to the different layers.

The figure also shows some streak-lines of the velocity field. Streak-lines represent the path that a particle would follow if the velocity field would be stationary. At a number of points within the basin, such streak-lines have been calculated. These points are also plotted, to give a sense of direction to the streak-line. In the upper layer, the general direction of the streak-lines is westward and most of the streak-lines end in a very narrow band near the

Configuration	$\boldsymbol{\theta_N}$	$\boldsymbol{\theta_S}$
A	53°N	10°S
B	$\langle 40\text{–}50 \rangle$°N	$\langle 20\text{–}10 \rangle$°S
C	$\langle 40\text{–}50 \rangle$°N	$\langle 15\text{–}5 \rangle$°S

Table 4.1: The different configurations for the θ_N and θ_S region.

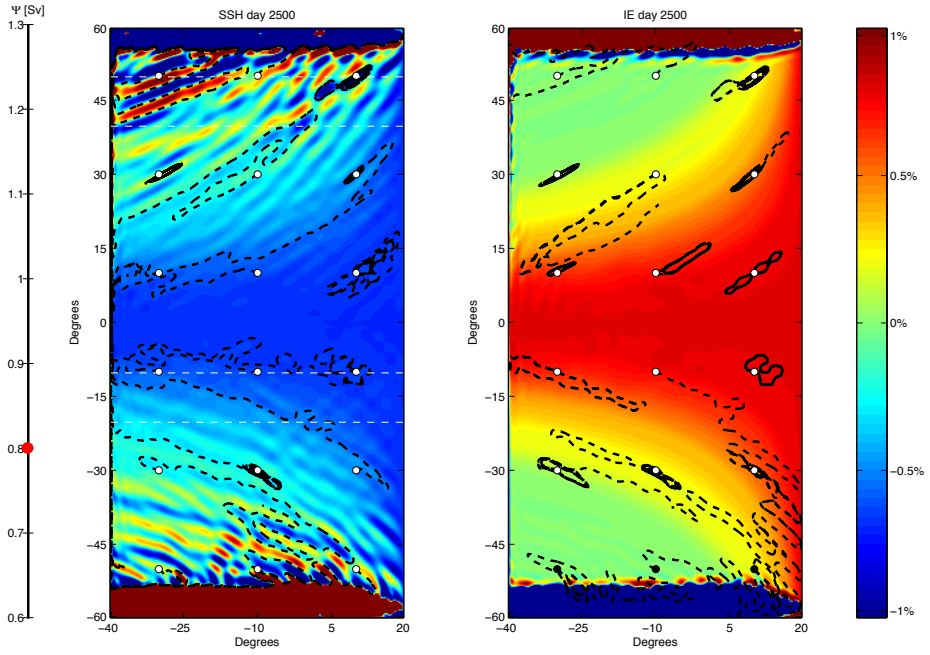

Figure 4.18: The overturning strength Ψ (left) and the SSH *and* IE *after 2500 days for the experiment where ΔP_{NS} is defined by the average* SSH *in the regions between the dashed white lines (configuration B). The scale is the same as for the snapshots of the Agulhas ring (*±5 mm *for the* SSH *and* ±2 m *for the* IE*). The figure also shows various streak-lines as calculated from the velocity fields. The streak-lines emerge at the white dots, and give some insight in the (instantanious) circulation in the different layers.*

western border. Apparently, most mass is transported through a very narrow boundary layer current close to the western border. This is also what has been found by Weijer et al. (2002).

On a more detailed level, however, the streak-lines are irregular. Apparently, the velocity field is not very coherent, allowing water particles to wander without much sense of direction through the basin more or less following the geostrophic contours. Especially on the interface, some water particles seem to be caught in mesoscale eddies, which are oblique and are aligned with the isopleths. There is some evidence, while comparing different snapshots, that at the interface these eddies are shed from the northern mass exchange region and slowly drift toward the western border of the equator. The snapshots of the SSH seem to support that, as positive elevation eddies can be monitored. This result is very intriguing, as it suggests that the adjustment to a changing overturning is not a continuous process, but occurs in eddies. This is similar to the exchange of water between the Indian and Atlantic Ocean, where the Agulhas rings are the

mesoscale eddies.

However, there is no evidence that this also occurs in nature. Since the model is highly idealized, and especially the implementation of the overturning is far from perfect (see section 3.6), it is more likely that this effect of eddy-shedding is an artifact from the model than undiscovered physics. Extra investigation into the process would take a different model, in which water particles can actually be followed. The streak-lines, which only give rough estimations of the flow field, can then be replaced by particle paths. However, this is beyond the scope of this thesis.

Returning to the figure, the mid basin SSH has dropped after 2500 days. The IE, on the other hand, has risen. This process is enhanced as the overturning circulation is further integrated. It is caused by an imbalance in the southern and the northern adjustment region. The maximum height anomaly in the southern adjustment region is much larger than that in the northern one. This is true for both the SSH and the IE. As the regions θ_N and θ_S are not symmetrically located around the equator, changes in the northern adjustment region are translated to changes in Ψ faster than changes in the southern adjustment region. Therefor, the overturning follows the northern mass exchange region closer than the southern region, and this allows for the southern region to grow larger than the northern one. As the total mass is conserved (even within a layer), this must result in a change of mean elevation outside the mass exchange regions.

One way to solve this is to shift the P_N region southward, but this will decrease the physical usefulness of the model. As was already stated, the region of downwelling should be placed as far northward as possible, and this was also the region on which Weijer et al. (2002) based their calculations. Moreover, the effect of the discrepancy between the northern and southern adjustment regions is basinwide. The effects on P_N and P_S are equal, as can already be observed in figure 4.16. The pressure in both regions drops with time, but as only the difference is required, this has no effect on ΔP_{NS}. We conclude that, although not elegant, the change in basinwide elevation is of minor importance to the results of the experiments to come.

The next experiment will investigate the impact of the Mid-Atlantic ridge on the overturning spin-up. Using the parameters of configuration C, an experiment has been conducted in a basin with a MAR. Surprisingly, the presence of the meridional obstacle does not seem to have much influence on the total overturning with time, as can be seen in figure 4.19. On a more detailed level, however, there are some significant differences. Already from initiation, the MAR-overturning slowly drops where the other overturning experiments remain at their initiation value. This implies that the MAR induces fast signals that can sooner influence the regions θ_N and θ_S. Since we are looking for fast responses, this is a hopeful result.

After approximately 800 days, the overturning strength drops significantly, as is also the case in the flat-bottom geometry. However, the minimum overturning strength is less pronounced in the experiment with the MAR. When the overturning accelerates again, after 5000 days, the noise on the MAR-experiment

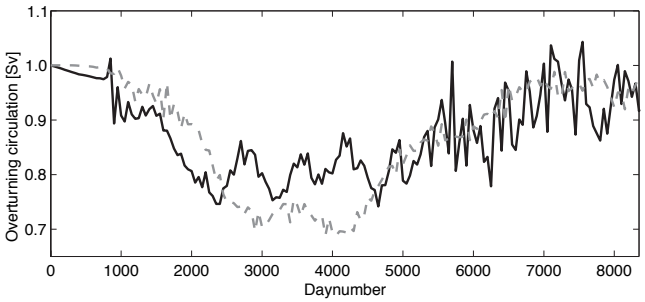

Figure 4.19: The overturning strength Ψ as a function of time for the experiment with a Mid-Atlantic Ridge (solid) and without (dashed, gray). The regions θ_N and θ_S are taken from configuration C.

is much larger than in the experiment without topography, despite the equivalent configuration of θ_N and θ_S. Apparently, the ridge distorts the signal, especially in the northern region. But apart from this enhancement in the level of variance, the last 3000 days of the model run are not significantly influenced by the presence of the MAR.

4.5.2 Flux driven circulation

The second implementation of a Meridional Overturning Circulation is the flux driven one, as discussed in section 3.6.2. Although the runs with the two parameterizations have been done using similar conditions, they are not of the same length. Due to a limit in computational time, the flux driven model implementation have only been run for 5000 days, instead of the 8000 days that were integrated in the pressure driven parameterization. As has already been noticed, the first 5000 days give a good impression of the overturning mechanisms. Moreover, the flux driven implementation has already spun up (equatorial transport equal to the overturning strength) after 2500 days.

The overturning strength as a function of time is plotted in figure 4.20. Both a run with a MAR and one without have been performed. There has been no additional tuning on the latitude over which the meridional fluxes are calculated. All runs use $\theta = 40°$N as this latitude.

The most striking difference between the two overturning implementations is the magnitude of the fluctuations. Where the pressure driven implementation resulted in an overturning which was never more than 0.5 Sv away from the initial 1 Sv bias, the flux driven implementation results in overturning strength reaching 6 Sv. Both the run with and without a MAR show an increase in the overturning strength from initiation on. It seems that the flux driven parameterization is more unstable in the sense that there is a positive feedback between the meridional fluxes and the overturning strength. It would be interesting to see whether the overturning reaches some equilibrium strength, but this can

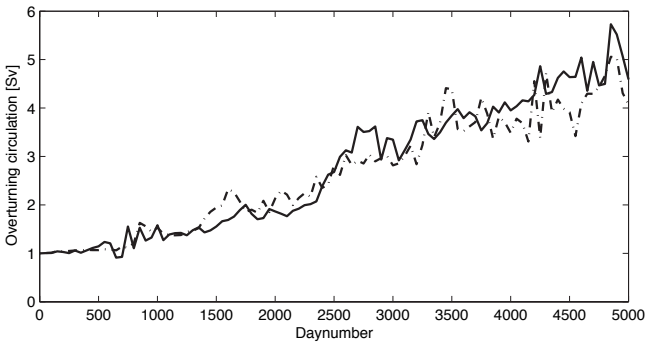

Figure 4.20: The overturning strength Ψ as a function of time for the experiment with a flux driven parameterization of the MOC. *The figure shows the results without a Mid-Atlantic Ridge (solid) and with (dashed) one.*

take weeks to months of computational effort. Unfortunately, that time is not available.

The fact that the overturning does not reach an equilibrium is unfortunate, but not insuperable. As shall be shown later, it is still possible to insert an Agulhas ring into the overturning circulation and draw conclusions from the changing overturning strength.

Although the magnitude of the overturning strength is much greater, the way in which the overturning is manifested in the basin is very similar to that of the pressure driven parameterization. The two mass exchange regions grow very large: the interface experiences a depression of 430 m after 5000 days in the run without a MAR. The interface and sea surface outside the mass exchange regions also rise and drop respectively, similar to the way these change in the pressure driven implementation. These large layer thickness changes can pose a problem. If the layer thicknesses alter too much, the linear theory on which all dynamical consideration are based does not hold any more. This is certainly the case in the mass exchange regions. Fortunately, the magnitude of the layer thickness change is only 7 m at maximum in the central basin, far away from the mass exchange regions. In this central basin, on which we focus during the discussion of the results, the linear theory still holds.

The circulation pattern (not shown) is similar to the one discussed in the previous section. On a macro-scale, the flow is westward in the upper layer, with a very narrow band of northward flow near the western coast. However, the streak-lines show meso-scale eddies slowly drifting from the region of mass input to the region of mass extraction.

There are no significant differences between the presence and absence of a MAR. As was already seen in the first parameterization, the ridge does not drastically influence the model spin-up and steady state.

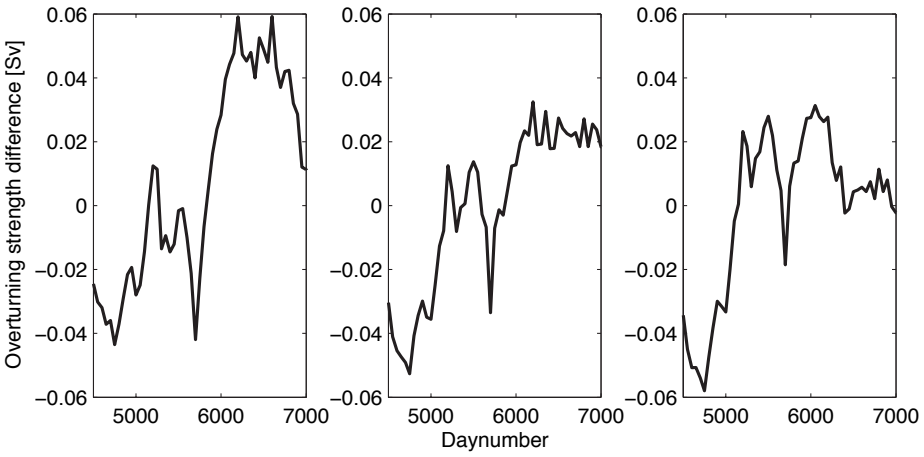

Figure 4.21: The 500 day moving average overturning strength difference $\tilde{\Psi}_{diff}$. The left figure shows configuration A, the figure in the center configuration B and the right figure depicts the experiment with configuration C.

4.6 Responses to an Agulhas ring

Now that the spin-up and steady state of the Meridional Overturning Circulation in the two different parameterizations have been discussed, we are able to focus on the responses of the MOC on an Agulhas ring.

4.6.1 Pressure gradient driven circulation

All three configurations discussed in section 4.5.1 can be used to facilitate an Agulhas perturbation. After 4500 days, that is, after the overturning has sufficiently spun up, a ring is released in the model. The ring is identical to that used in the Two Layer experiment of section 4.3. The ring drastically alters the overturning at a relatively high frequency, in the order of months. In order to suppress this high frequency modification, the figures are shown as moving averages over 500 days. In this way, they are smoothed and the qualitative results can be more appreciated. As the data is provided every 50 days, the moving average can be calculated by using

$$\tilde{\Psi}(t) = \frac{1}{11} \sum_{\tau=-5}^{5} \Psi(t-\tau) \tag{4.12}$$

Figure 4.21 shows how the overturning strength is altered by an Agulhas ring for the three configurations discussed in the previous section (table 4.1). The plots show the change in overturning strength when a ring is released relative

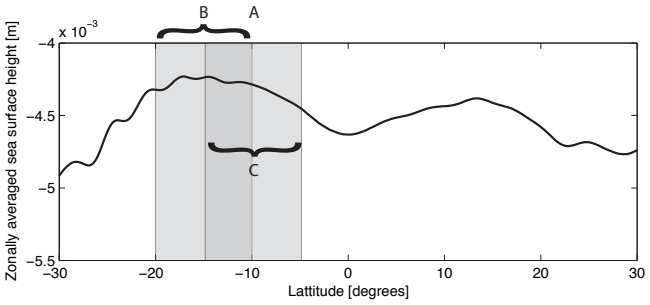

Figure 4.22: The zonally averaged sea surface elevation near the equator after 6500 days (2000 with a perturbation) in the experiment with configuration B. The letters show θ_S for the different configurations. Only configuration C is influenced by the equatorial current zone.

to the unperturbed situation.

$$\Psi_{\text{diff}} = \Psi_{\text{Ring}} - \Psi_{\text{NoRing}} \tag{4.13}$$

In general, the following response can be observed: Initially, the overturning strength difference drops. This is due to the definition of the overturning strength, equation 3.28. The perturbation is a positive pressure anomaly, and as it is released in the Southern hemisphere, we can expect P_S to rise earlier and more than P_N. This causes ΔP_{NS} to drop and thereby it reduces the overturning circulation strength Ψ.

After this initial drop, the overturning strength difference starts to rise. This is the time that also P_N gets affected by the Agulhas ring, mostly through barotropic adjustment. At day 5800, 1300 days after the ring is released, the overturning strength difference suddenly drops again. At this time, the ring arrives at the western coast of the Southern Atlantic, and a coastal Kelvin wave is formed. This Kelvin wave crosses the region where P_S is computed on its way to the equator (remember that θ_S is always between the release latitude 30°S and the equator), and the pressure P_S will rise again. This results in a drop in the overturning strength. When this short event has occurred, the overturning strength starts to rise again.

The three experiments differ in the behavior after the moment that the equatorial Kelvin current has transported the pressure anomaly to the eastern coast. The first two experiments show a positive overturning strength difference. The last one, in which θ_S extends far within the equatorial region, shows a reduction is the overturning strength at day 6500. An explanation for this is that the equatorial currents keep the sea surface height low, compared to the SSH further from the equator. As P_S is low, the overturning strength is suppressed and the rise in P_N can not compensate for this. This reasoning again illustrates the strong dependency of the overturning strength on the choice for P_N and P_S. The situation is depicted in figure 4.22. Indeed, at day number 6500 (2000 days after the ring is released) the zonally averaged SSH shows a depression around

the equator.

Because of the application of a moving average, it is difficult to say something quantitatively about figure 4.21. However, all three experiments show that the effect of an Agulhas ring on the overturning is in the order of 0.05 Sv, both in the suppression halfway and the enhancement at the end of the model runs.

One could argue that the time at which the Agulhas ring is released, after 4500 days, is arbitrary and can have much effect on the out-comings of the experiments. Figure 4.17 indeed shows that after 4500 days, the overturning circulation is at its minimum strength and that there might be no evidence that the overturning is in equilibrium. In order to investigate this, one additional experiment has been performed.

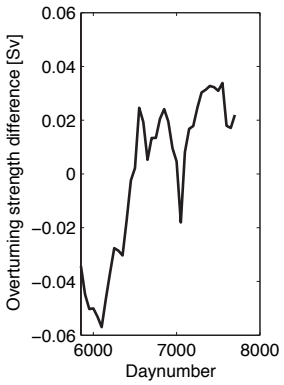

Figure 4.23: The moving average $\tilde{\Psi}_{diff}$ for configuration C, started after 5850 days.

Figure 4.23 shows the response of the overturning strength to an Agulhas ring released after 5850 days. Although the overturning strength is at this time still not stationary, the variability is much smaller. However, the qualitative discussion does not differ from the earlier one. Again, Ψ_{diff} initially drops to rise again in the next 1500 days.

At that time, the ring has crossed the Southern Atlantic and the coastal Kelvin current causes a reduction in Ψ_{Ring}. Finally, the overturning strength is somewhat enhanced in the last 800 days compared to the unperturbed situation. This provides support for the argument that the date of initiation does not influence the qualitative response of the overturning circulation.

Now that the release of an Agulhas ring in a model with flat-bottom geometry has been discussed, it is possible to see what the influence of a MAR is on the response of an Agulhas ring. This is depicted in figure 4.24.

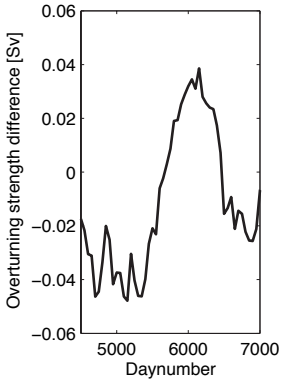

Figure 4.24: The moving average $\tilde{\Psi}_{diff}$ for configuration C and a Mid-Atlantic Ridge.

The responses to an Agulhas perturbation are identical, despite the presence of a MAR. Overturning is suppressed the first 1500 days, to be enhanced for the next 1000 days. This is the same behavior as was seen before. The only difference lies in the sudden suppression of the overturning strength after 1500

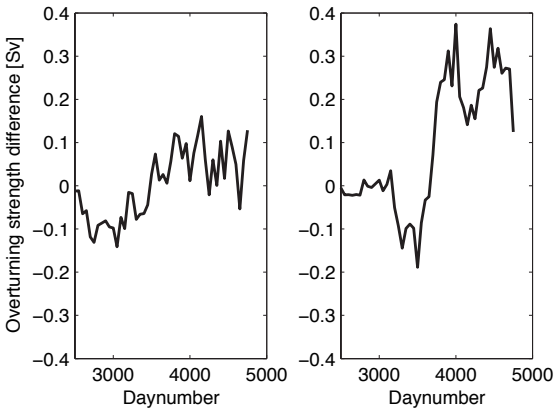

Figure 4.25: The 500 day moving average overturning strength $\tilde{\Psi}_{diff}$ for the flux driven parameterization. The left plot shows the results of the experiment without a Mid-Atlantic Ridge, the right one of the experiment with a Ridge.

days, which is absent in the experiment with a ridge. Apparently, the MAR can deform the ring in such a way that the western coastal Kelvin wave, and thereby the decrease in P_S, is less pronounced. But that is a short time-scale effect, on the long scale, the response does not seem to be altered by the presence of a topographic ridge. Even the quantitative behavior of the response, approximately 0.05 Sv, is not changed by the ridge.

4.6.2 Flux driven circulation

The introduction of an Agulhas Ring into the overturning circulation governed by a flux driven parameterization shall now be discussed. It was already mentioned that the overturning in the flux driven parameterization achieves a steady state much sooner than the other parameterization. After 2500 days the overturning strength and the transport over the equator are equal, implying a matured overturning circulation. It is therefor possible to release the perturbation after 2500 days of integration, as opposed to the 4500 days of spinning up in the pressure gradient driven implementation.

The response of the overturning strength on the introduction of an Agulhas ring is shown in figure 4.25. The left figure reveals the response on the overturning without a Mid-Atlantic Ridge, and the right one shows the response in the basin configuration with such a MAR.

The flat-bottom model run does not show a large response, the largest magnitude of the difference between the perturbed and unperturbed run being 0.15 Sv. However, this is 3 times larger than the maximum response in the pressure gradient parameterization. Much larger responses can be seen in the model configuration with a MAR. Initially, the response can almost be neglected. But when the ring arrives at the Brazilian coast, the overturning strength is increased by

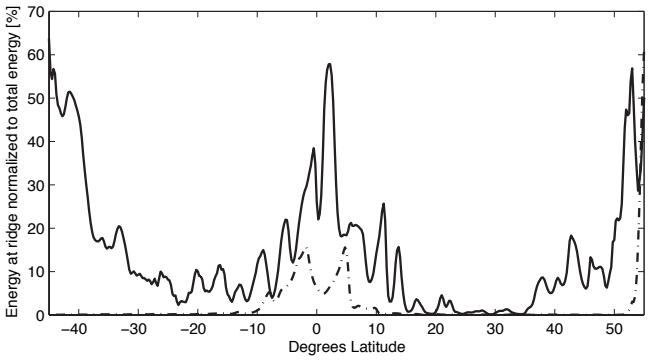

Figure 4.26: The baroclinic energy over the domain 15°W–5°W as a function of latitude. The energy has been normalized to the total zonal baroclinic energy to yield a percentage. The figure shows the results for the experiment with an Agulhas ring after 4500 days with a MAR *(solid) and without such a ridge (dash-dotted).*

almost 0.4 Sv compared to the unperturbed situation. This response is 8 times larger than in the previous parameterization.

The sign of the response (an increase in overturning strength) can be understood. As was already noted in section 3.6.2, it is only the baroclinic signal that can alter the overturning strength in this parameterization. From initiation, the ring already inhabits a baroclinic component. As the mass and energy is transported north, this baroclinic mode will also gain a northward component, enhancing the northward upper layer flux and thereby the overturning strength.

The response is much greater when a MAR is included in the basin, than when it has been left out. Apparently, the capability of the ridge to act as a guide for baroclinic energy is important for the magnitude of the response. Not only the western boundary layer, but also the ridge can act as a waveguide. The ring energy can be transmitted by both the western boundary layer current and the topographic Rossby waves. This behavior can also be observed in the pressure gradient driven implementation.

Figure 4.26 shows the baroclinic kinetic energy that is available in the center of the basin. The energy between 15°W and 5°W at a given latitude is normalized to the total baroclinic energy over that latitude. The equatorial waveguide is clearly visible as a maximum in energy near the equator. The figure supports the idea of an extra baroclinic energy guide along the MAR. The energy available at mid-basin in this experiment is much larger than when the ridge is absent. While the area encompasses only 16% (10° of the zonal domain), the energy at these longitudes can be as high as 60% of the total energy. Especially near the equator and the regions of mass exchange, therefor, the MAR must be considered a very good attractor of baroclinic energy.

The figure also shows that north of 10°N only little baroclinic energy is present at the Mid-Atlantic ridge. In the theoretical discussion of topographic Rossby waves, it has been shown that these waves can pass the equator, but

only to approximately 10°N. After that, the sign of the group velocity changes and the waves will be halted. The energy will be radiated west- and eastward as normal Rossby waves. This mechanism is supported by the results found in this figure. There is a large increase of energy at the MAR north of 35°again. This is the extra energy that causes the enhancement of the overturning strength seen in figure 4.25. It is absent when there is no MAR, supporting the crucial role of the waveguide. The small bulks of energy between 15°N and 35°N are solitary Rossby wave packages, which slowly travel northward. Although they resemble only 5% of the total zonal energy, they transport enough baroclinic energy northward to have a large effect on the overturning strength.

Chapter 5

Discussion

5.1 The model

Before discussing the results and the implications of these, the first question to be asked is whether the model gives a trustworthy representation of the physical processes that it is designed for to capture. This has partly already been discussed in the previous chapter, but no conclusions have been drawn yet.

The behavior of the ring seems to be reasonably consistent and appropriate for a true Agulhas ring. The expectations from knowledge of Kelvin and Rossby waves have been met. However, the stability of the ring may be considered too large. In the Atlantic Ocean, most rings decay faster than is the case in this implementation. De Steur et al. (2004) shows that the resolution in the model is too course to enable the generation of instabilities. This can be a significant effect, especially since a disintegrated ring might not provide for strong western coastal Kelvin currents, equatorial Kelvin currents and Rossby basin modes, all of which are crucial for the answer to our research question.

The Meridional Overturning Circulation (MOC) is less consistent with what is encountered in nature. The magnitude of the bias in the experiments (1 Sv) is far smaller than the true overturning strength. Also the fact that for both implementations the mean elevation outside the regions of mass exchange changes with time is not very realistic. It has already been noted that this effect is of minor importance to the calculation of the overturning strength Ψ, but it certainly does not increase the faith in a good representation of the MOC. A problem in that context is that there are no references of a MOC in a Two-Layer model. It is therefor unknown whether this model behaves better or worse than similar models designed by others. Moreover, we do not even know whether it is possible at all to include a MOC in a TL-model. In general, thermohaline processes are required to transport mass between layers and to change water masses. Much more research has to be done on this part since a adequate parameterization of the MOC in a TL-model might provide the scientific community with a useful additional tool to study an important process in the global ocean

circulation.

The regions of mass exchange, which have been used in both parameterizations, can be subject to discussion as well. The implementation is far from ideal, with extreme interface rises and drops. The circulation in these regions has not been discussed as it shows extreme (anti)cyclonic currents around the perturbations. Velocities are many orders of magnitude larger than in the rest of the basin. But even if the implementation would improve, the location of the regions can still be disputed. In this research, they span the entire width of the basin, whereas in nature both down- and upwelling occur at relatively localized regions. It is unclear what the effect of other mass exchange regions is on our results.

The first parameterization, the use of the linear relationship between overturning strength and the meridional pressure gradient can also be questioned. It was already noted that for a ring to influence the MOC, it has to have a significant baroclinic component. This baroclinic energy can then alter the overturning through its shear. But using the relation found by Weijer et al. (2002) requires only integration over the upper 500 m of the ocean. This integration does therefor not incorporate any information on the baroclinic energy of the system, as it does not distinguish between barotropic and baroclinic modes. This is a serious drawback, as this argument weakens one of the fundamental ideas of this research. The advantage of the parameterization, however, is that it is founded on prior results. Although is can be disputed, there is some relation with other scientific research.

The second parameterization is not perfect either. The highly idealized conceptual model of the overturning circulation does not incorporate any physical mechanisms that can be related to the mass exchange. The advantage, however, is that only the baroclinic signals are taken into account. This is a better representation of the real-world overturning, which is a baroclinic process. Another advantage is that the implementation requires less a priory choices of parameters. Only the calculation latitude, θ_N has to be chosen, as opposed to the parameters c, θ_N and θ_S that are required for the pressure gradient driven parameterization of the overturning circulation.

In view of this, it was also a problem that the computational power available was limited. A run of the overturning, 8000 days, took approximately 2 weeks of computational time. This was a serious limitation in the ability to tune the parameters and thereby get more acquainted with the features of the model. However, this could have been improved by using a mode-splitting in the model implementation. An implementation in which the baroclinic mode is only calculated every $\mathcal{O}(50)$ barotropic time steps is much faster.

5.2 The results

From the results of our experiments, it can be concluded that the time scale of the response of the MOC on an Agulhas ring is approximately 1000 days (3 years). This is equal to the time it takes for the Agulhas ring to cross the South

Atlantic Ocean, and it is therefor tempting to say that this crossing of the ocean is the key role in the response. However, there have been no tests with rings released at other locations, and the two results can therefor not with absolute certainty be linked. But as there is a physical basis on which the coincidence of the arrival of the ring at the Brazilian coast and the response of the MOC can be founded, evidence points towards this conclusion.

The role of the Mid-Atlantic Ridge in a possible shortening of the response time of the MOC is unclear. There has been little evidence in the results that give the MAR a significant role in the response. However, the interaction between a barotropic Rossby wave and a meridional ridge is still not fully understood. From these experiments, it seems that only a relatively small portion of the barotropic energy is converted into free baroclinic Rossby waves by the ridge. The only conversion that can be identified is that from barotropic waves into baroclinic topographic waves.

In the quantitative sense, the response in the pressure gradient driven parameterization has been limited. The responses that are produced by the model are small, in the order of 0.05 Sv, which is insignificant in comparison to a 15–20 Sv overturning in nature.

The responses in the flux driven parameterization have been larger, up to 0.4 Sv. It is therefor tempting to say that this parameterization is better than the pressure gradient driven one. However, one should be careful with such statements. As the basis of the two parameterizations is different, it is very difficult to compare them. Especially since the true response is poorly know.

Although the results have not been shown in the previous chapter, additional experiments have been performed to investigate whether a higher Mid-Atlantic Ridge could increase the response. Doubling the maximum MAR height to 2 km (and decreasing the lower layer depth over the ridge from 3 km to 2 km) did not significantly change the dynamics of a ring as has been discussed for a 1 km high topographic ridge. The use of a Gaussian shaped ridge did not alter the dynamics either. It seems that the shape and size of the ridge is of minor importance.

Experiments have also been conducted in which the size of the ring was changed, or where multiple rings were placed on a lattice. The objective was to force longer barotropic Rossby waves, with a westward group velocity. These waves could then transport barotropic energy from the Cape of Good Hope towards the Mid-Atlantic Ridge, shortening the time it takes for the ring to arrive at the MAR. All configurations did not show any significant alteration in the dynamical properties of the ring. This can be understood from the fact that the wave envelope moves with βR_d^2 independent of the wave length of the Rossby waves (Longuet-Higgins, 1965).

From very basic calculations, one could already have seen that the *direct* response is not very large. At the surface, the extra water that is brought into the basin by an Agulhas ring is (refer to equation (4.1)) $M_p = 2.0 \cdot 10^{10}$ m^3. If this was to be used as a significant amount of extra overturning strength (a 0.5 Sv anomaly), it would have to be formed into North Atlantic Deepwater within $4 \cdot 10^4$ s, i.e. less than 12 hours. This is an unphysically short time-span

for the excess water in the ring to have a direct effect.

This leaves the indirect effect. One could expect that the presence of a ring in a dynamically not very stable environment as the MOC, can have great implications. But from sensitivity studies on the MOC in this model, it seems that the large-scale picture of overturning behavior in this model is not as unstable as one would imagine it to be. It seems that the MOC is too robust for an Agulhas ring to have much effect via some indirect mechanism. The evidence behind this is that all runs of the MOC, with different parameters, give a comparable result of the long-time scale behavior. In some sense, this is a positive comment, as it provides extra trust in the fact that the representation of the MOC is correct. However, the large difference in effects between the two parameterization largely cancels this trust.

The research question on page 4 is formulated in terms of response times. The question is therefor what the temporal scale of the response is. In all experiments, using both parameterizations, it has been shown that at the moment that the Agulhas ring reaches the coast of South-America, the response suddenly changes. This happens approximately 1000 days after the ring has been released. This date can be considered as the divider between two regimes, the short-term decrease in overturning strength before and the long-term increase after it.

One of the differences between the two parameterizations is that the flux driven one is confined to processes on the northern hemisphere, whereas the pressure gradient driven one is also directly affected by changes in the southern hemisphere ocean. As the short-term changes (i.e. in less then 1000 days) occur mostly in the pressure gradient driven parameterization, this gives rise to a division in responses in the southern hemisphere on the short time-scale, and responses in the northern hemisphere which occur on the longer time-scale. This is not very strange, as the ring mass and energy reach the northern hemisphere mainly by the equatorial Kelvin current which manifests itself only after the ring has travelled towards the western border.

From this discussion, it might be concluded that the ability of a ring to reach the South-American coast as a coherent structure is of crucial importance to the forcing it can have on the overturning circulation. Unstable rings that disintegrate well before reaching the coast (which is the majority of the rings in nature) may induce a smaller mass and energy transfer and might therefor lack the positive effect on the overturning strength after 1000 days. On the other hand, the baroclinic Rossby waves that are the result of the disintegration of the Agulhas ring might arrive at the western coast sooner. The response will then be not as abrupt as in the case with a coherent ring, but the response time might even decrease. It might therefor be interesting to further study the relation between the stability (ability to travel across the Atlantic) of a ring and its forcing on the MOC, both with numerical studies and oceanographic data analysis.

What can be said about the responses in nature? The model lacks currents

and winds. Topography and bathymetry are highly idealized. Moreover, only one ring is concerned in the model runs. In reality, some six rings are shed every year. This implies that during the model simulations (2500 days), some 40 rings may have been released into the Atlantic Ocean. This can change the response time, as one can imagine that 40 rings may have a different result on the MOC.

It might therefor be worthwhile to invest in a more realistic study of the interaction of Agulhas rings on the MOC. This can be done by using a (coupled) GCM with a good representation of the frequency at which the Agulhas rings are formed. It might be that the responses will then be more significant.

Chapter 6

Conclusions

The model as used in this research project is both robust and simple, and can be used to investigate subtle processes of which the theoretical background has not been understood. The model does therefor provide an adequate tool to study the complex dynamics of the response of the Meridional Overturning Circulation to an Agulhas ring.

The implementation of an Agulhas ring into a Two-Layer model has been successful. The ring behaves adequately when compared with oceanographic field data. The path and drop of maximum sea surface height are according to what has been observed in nature. The way in which the energy and mass is transported around the basin is in good agreement with what the theory predicts. However, there are also some features that are not understood. The enhanced zonal velocity of the ring in a TL-model configuration and the dependence of the equatorial waveguide on the presence of a Mid-Atlantic Ridge are two of those.

Using the results that are produced by the model, the research questions as posed in the introduction can to some extent be answered. According to the model, the MOC responds to the introduction of an Agulhas ring after 1000 days. The magnitude of the response depends on the implementation of the overturning strength chosen. The parameterization of this physical mechanism is therefor the key issue of this research project.

For this reason, two different implementations of the overturning circulation in the Two-Layer model have been developed. Both are highly idealized, but the fact that they sprung from very different assumptions makes them able to reinforce each other. This gives extra confidence to a feature that can be identified in both implementations.

One feature that the two implementations share is the division between a negative response (decrease of the overturning strength) on the short time scale and a positive response on the longer time scale. The border between those regimes lies 1000 days after the Agulhas ring has been released. At this time, the ring has zonally traversed the South Atlantic Ocean and has arrived at the South-American coast. The results therefor provide for evidence that the

Meridional Overturning Circulation responds within approximately 3 years on an Agulhas ring.

The magnitude of the response, in contrast to the direction, is different in the two parameterizations. A flux driven parameterization gives significant responses of up to 0.4 Sv per ring. A pressure gradient driven parameterization gives much smaller responses, which are only 0.05 Sv per ring.

Many dynamical properties of the model have been in accordance to theoretical predictions. The sequence westward Rossby wave, western border equatorward Kelvin wave, equatorial Kelvin wave, eastern border poleward Kelvin wave and westward Rossby wave of the travelling Agulhas ring has been seen in other studies, as well as field experiments. The western boundary layer intensified northward flow in the upper layer of the Meridional Overturning Circulation has also been observed previously.

The dynamical properties of the MOC away from the boundary layer however, have not been seen before. The meso-scale eddies that emerge from the mass exchange regions in this model are artifacts of the model implementation. These eddies are also the cause of the amount of noise on the overturning signal, forcing data-smoothing methods to be used in the interpretation of the results.

Returning to the third of the research questions on page 4, the presence of a Mid-Atlantic Ridge is of limited influence to the response of the overturning circulation. The response time is not significantly altered. It appears that the MAR plays no role in transforming barotropic energy into baroclinic, thereby shortening the response time. The only influence that has been found is the capability of the ridge to act as a waveguide for topographic Rossby waves. In this way it provides for an extra way to transport mass and energy northward. However, due to the radiation of free Rossby waves from the ridge, the waveguide is not very effective. The role of the MAR is therefor limited in the response of the overturning circulation on an Agulhas ring.

Acknowledgements

I would like to thank Peter Jan van Leeuwen for his ideas and guidance throughout my master thesis project. The way in which he subtly acted at the background was very inspiring for me. I would like to thank Henk Dijkstra for being the second referee of this thesis on such short notice and giving useful feedback. I would also like to thank Lianke ter Raa for useful comments on the pressure gradient driven parameterization. Finally, I would like to thank Judith, for her tremendous support and patience.

Bibliography

Anderson, D. and Rowlands, P. (1976). The role of inertia-gravity and planetary waves in the response of a tropical ocean to the incidence of an equatorial Kelvin wave on a meridional boundary. *Journal of Marine Research*, 34(3):295–312.

Andersson, H. and Veronis, G. (2004). Thermohaline circulation in a two-layer model with sloping boundaries and a mid-ocean ridge. *Deep-Sea Research I*, 51:93–106.

Clark, P., Pisias, N., Stocker, T., and Weaver, A. (2002). The role of the thermohaline circulation in abrupt climate change. *Nature*, 415:863–869.

De Ruijter, W., Biastoch, A., Drijfhout, S., Lutjeharms, J., Matano, R., Pichevin, T., Van Leeuwen, P. J., and Weijer, W. (1999). Indian-Atlantic interocean exchange: dynamics, estimation and impact. *Journal of Geophysical Research*, 104(C9):20,885–20,910.

De Steur, L. (2005). *Stirred, not mixed : a study on the decay of Agulhas rings*. PhD thesis, Utrecht University.

De Steur, L., Van Leeuwen, P. J., and Drijfhout, S. (2004). Tracer leakage from modelled Agulhas rings. *Journal of Physical Oceanography*, 34(6):1387–1399.

Drijfhout, S., Katsman, C., De Steur, L., Van der Vaart, P., Van Leeuwen, P. J., and Veth, C. (2003). Modeling the initial, fast sea-surface height decay of Agulhas ring "Astrid". *Deep-Sea Research II*, 50:299–319.

Ganachaud, A. and Wunch, C. (2000). Improved estimates of global ocean circulation, heat transport and mixing from hydrographic data. *Nature*, 408:453–456.

Gill, A. (1982). *Atmosphere-Ocean Dynamics*, volume 30 of *International Geophysics Series*. Academic Press.

Gordon, A. (1986). Interocean exchange of thermocline water. *Journal of Geophysical Research*, 91(C4):5037–5046.

Hibiya, T., Nagasawa, M., and Niwa, Y. (1999). *Dynamics of oceanic internal gravity waves II, Proc. 'Aha Huliko'a Hawaiian Winter Workshop*, chapter Model predicted distribution of internal wave energy for diapycnal mixing processes in the deep waters of the North Pacific, pages 205–213. SOEST Publications, Honolulu.

Holton, J. (1992). *An Introduction to Dynamic Meteorology*. Number 48 in International Geophysics Series. Academic Press.

IPCC (2001). *Climate Change 2001: Synthesis Report*. Cambridge University Press.

Johnson, H. and Marshall, D. (2002a). Localization of abrupt change in the North Atlantic. *Geophysical Research Letters*, 29(6):7–1–7–4.

Johnson, H. and Marshall, D. (2002b). A theory for the surface Atlantic response to thermohaline variability. *Journal of Physical Oceanography*, 32:1121–1132.

Kamenkovitch, V., Leonov, Y., Nechaev, D., Byrne, D., and Gordon, A. (1996). On the influence of bottom topography on the Agulhas eddy. *Journal of Physical Oceanography*, 26(6):892–912.

Kantha, L. and Clayson, C. (2000). *Numerical Models of Oceans and Oceanic Processes*. Academic Press.

Knorr, G. and Lohmann, G. (2003). Southern Ocean origin for the resumption of Atlantic thermohaline circulation during deglaciation. *Nature*, 424:532–536.

Kowalik, Z. and Murty, T. (1993). *Numerical modelling of ocean dynamics*. Number 5 in Advanced Series on Ocean Engineering. World Scientific.

Levitus, S. (1982). *Climatological atlas of the world ocean*. U.S. Government Printing Office.

Liu, Z., Wa, L., and Baler, E. (1999). Rossby wave-coastal Kelvin wave interaction in the extratropics. part I: Low-frequency adjustment in a closed basin. *Journal of Physical Oceanography*, 29:2382–2404.

Longuet-Higgins, M. (1965). The response of a stratified ocean to stationary or moving wind-systems. *Deep-Sea Research*, 12:923–973.

Mesinger, F. and Arakawa, A. (1976). *Numerical methods used in atmospheric models*. Number 17 in GARP Publications. World Meteorological Organization.

Munk, W. and Wunch, C. (1998). Abyssal recipes II: energetics of tidal and wind mixing. *Deep-Sea Research I*, 45:1977–2010.

Pedlosky, J. (1987). *Geophysical Fluid Dynamics*. Springer.

Peeters, F., Acheson, R., Brummer, G., De Ruijter, W., Schneider, R., Ganssen, G., Ufkes, E., and Kroon, D. (2004). Vigorous exchange between the Indian and Atlantic oceans at the end of the past five glacial periods. *Nature*, 430:661–665.

Rahmstorf, S. (1996). On the freshwater forcing and transport of the Atlantic thermohaline circulation. *Climate Dynamics*, 12:799–811.

Rahmstorf, S. and Ganopolsky, A. (1999). Long-term global warming scenarios computed with an efficient coupled climate model. *Climatic Change*, 43:353–367.

Schouten, M., De Ruijter, W., and Van Leeuwen, P. J. (2002). Upstream control of Agulhas ring shedding. *Journal of Geophysical Research*, 107(C8).

Schouten, M., De Ruijter, W., Van Leeuwen, P. J., and Lutjeharms, J. (2000). Translation, decay and splitting of Agulhas rings in the southeastern Atlantic Ocean. *Journal of Geophysical Research*, 105(C9):21913–21925.

Van Aken, H., Van Veldhoven, A., Veth, C., De Ruijter, W., Van Leeuwen, P. J., Drijfhout, S., Whittle, C., and Rouault, M. (2003). Observations of a young Agulhas ring, Astrid, during MARE in March 2000. *Deep-Sea Research II*, 50:167–195.

Van Leeuwen, P. J., De Ruijter, W., and Lutjeharms, J. (2000). Natal pulses and the formation of Agulhas rings. *Journal of Geophysical Research*, C3:6425–6436.

Weijer, W., De Ruijter, W., Dijkstra, H., and Van Leeuwen, P. J. (1999). Impact of interbasin exchange on the Atlantic overturning circulation. *Journal of Physical Oceanography*, 29:2266–2284.

Weijer, W., De Ruijter, W., Sterl, A., and Drijfhout, S. (2002). Response of the Atlantic overturning circulation to South Atlantic sources of buoyancy. *Global and Planetary Change*, 34:293–311.